Carbon Outgassing in the Antarctic Circumpolar Current Is Supported by Ekman Transport From the Sea Ice Zone in an Observation-Based Seasonal Mixed-Layer Budget

Jade Sauvé[1] , Alison R. Gray[1] , Channing J. Prend[1,2] , Seth M. Bushinsky[3] , and Stephen C. Riser[1]

[1]School of Oceanography, University of Washington, Seattle, WA, USA, [2]Environmental Science and Engineering, California Institute of Technology, Pasadena, CA, USA, [3]Department of Oceanography, School of Ocean and Earth Science and Technology, University of Hawaii at Manoa, Manoa, HI, USA

Abstract Despite its importance for the global cycling of carbon, there are still large gaps in our understanding of the processes driving annual and seasonal carbon fluxes in the high-latitude Southern Ocean. This is due in part to a historical paucity of observations in this remote, turbulent, and seasonally ice-covered region. Here, we use autonomous biogeochemical float data spanning 6 full seasonal cycles and with circumpolar coverage of the Southern Ocean, complemented by atmospheric reanalysis, to construct a monthly climatology of the mixed layer budget of dissolved inorganic carbon (DIC). We investigate the processes that determine the annual mean and seasonal cycle of DIC fluxes in two different zones of the Southern Ocean—the Sea Ice Zone (SIZ) and Antarctic Southern Zone (ASZ). We find that, annually, mixing with carbon-rich waters at the base of the mixed layer supplies DIC which is, in the ASZ, either used for net biological production or outgassed to the atmosphere. In contrast, in the SIZ, where carbon outgassing and the biological pump are weaker, the surplus of DIC is instead advected northward to the ASZ. In other words, carbon outgassing in the southern Antarctic Circumpolar Current (ACC), which has been attributed to remineralized carbon from deep water upwelled in the ACC, is also due to the wind-driven transport of DIC from the SIZ. These results stem from the first observation-based carbon budget of the circumpolar Southern Ocean and thus provide a useful benchmark to evaluate climate models, which have significant biases in this region.

Plain Language Summary The ocean surrounding the frozen continent of Antarctica plays an important role in the global cycling of carbon and is important for the climate of our planet. Despite its importance, there are gaps in our knowledge due to the difficulties involved in collecting data from a remote, seasonally ice-covered ocean. In this study, we use year-round data collected by autonomous instruments that can even measure under sea ice. We build a budget of carbon in the surface layer of the ocean, quantifying the different sources and sinks of inorganic carbon. We find that carbon mostly enters the surface layer through mixing with carbon-rich waters below. In the more stormy, northern part of our study area, this carbon is then either consumed by photosynthesis in the ocean or it is transferred to the atmosphere. In the southernmost region, biological activity and gas transfer at the ocean-atmosphere interface is hindered by the presence of sea ice and the surplus of carbon is instead transferred north by wind-driven circulation. Our results show that year-round measurements of carbon are necessary to understand carbon cycling in the region and we provide a useful product to compare to global simulations of the Earth system.

1. Introduction

The Southern Ocean plays a significant role in the global carbon cycle. Around 40% of oceanic uptake of anthropogenic carbon dioxide (CO_2) occurs in the waters south of 35°S (DeVries, 2014). Ekman divergence driven by strong westerly winds leads to a combination of upwelling and downwelling of natural and anthropogenic carbon, respectively. Consequently, the Southern Ocean is a strong CO_2 sink between 35 and 55°S, although the picture is not as clear at higher latitudes (Gruber et al., 2019). Historically, observations from this remote region have been strongly biased towards summer and limited spatially, particularly in the seasonally ice-covered areas. Data from autonomous biogeochemical floats deployed by the Southern Ocean Carbon and Climate Observations and Modeling (SOCCOM) project showed a stronger wintertime outgassing of carbon dioxide at high latitudes than expected, leading to a low Southern Ocean annual mean carbon uptake (Bushinsky et al., 2019;

Writing – original draft: Jade Sauvé
Writing – review & editing: Jade Sauvé,
Alison R. Gray, Channing J. Prend, Seth
M. Bushinsky, Stephen C. Riser

Gray et al., 2018). However, another recent study based on airborne measurements found strong Southern Ocean annual mean carbon uptake (Long et al., 2021).

Air-sea carbon fluxes are computed from the difference in CO_2 partial pressure (pCO_2) between the atmosphere and the ocean multiplied by a gas transfer velocity and the solubility of CO_2 in the ocean (Gray et al., 2018; Gruber et al., 2019). Since these last two parameters are strictly positive, the sign of the air-sea flux depends solely on the air-sea gradient in pCO_2. Spatio-temporal variability in atmospheric CO_2 is small compared to variability in surface ocean pCO_2 (Takahashi et al., 1997). Therefore, oceanic pCO_2 primarily determines seasonal and regional variations in air-sea carbon fluxes (Takahashi et al., 2002).

The dominant mode of variability for both surface ocean pCO_2 and air-sea carbon flux is the seasonal cycle (Gruber et al., 2019). Seasonal changes in ocean pCO_2 can be separated into thermal and non-thermal components using the well-known thermal sensitivity of pCO_2 (Takahashi et al., 1993). The thermal component is in phase with seasonal temperature changes. Colder waters have a higher dissolved carbon solubility leading to lower pCO_2 for the same amount of dissolved carbon dioxide. The non-thermal component is dominated by changes in dissolved inorganic carbon (DIC), and thus peaks in winter due to respiration and entrainment of subsurface carbon (Takahashi et al., 2002). South of the Sub-Antarctic front, pCO_2 seasonality is driven primarily by the non-thermal component (Gruber et al., 2019; Prend, Hunt, et al., 2022). Therefore, surface DIC variability is central to understanding high-latitude Southern Ocean air-sea carbon fluxes.

In order to understand air-sea carbon flux variations, it is useful to quantify the processes that alter mixed-layer DIC concentration. A range of tracer budgets have been used for this purpose across diverse space and time scales. As the necessary data is more readily available, there have been numerous DIC budgets constructed from model output, including from coupled models (Dufour et al., 2013; Hauck et al., 2013; Levy et al., 2013), idealized models (Bronselaer et al., 2018) and data-assimilating models (Carroll et al., 2022; DeVries, 2014; Jersild & Ito, 2020; Rosso et al., 2017). However, these model-based budgets often average the entire ocean south of a given latitude (usually 44°S) and are computed over a fixed depth. These modeling studies show that both biological and physical processes drive DIC variations, but no clear quantitative agreement has been reached about the leading order terms. In the high-latitude Southern Ocean, a small number of observation-based DIC budgets have been constructed using mooring data (Yang et al., 2021), shipboard sections (Brown et al., 2015; Jouandet et al., 2008; McNeil & Tilbrook, 2009; Munro et al., 2015), autonomous float data (Prend, Gray, et al., 2022; Williams et al., 2018) or a combination of methods (Merlivat et al., 2015; Shadwick et al., 2015). However, the limited number of studies, as well as the different characteristics of the budgets constructed, preclude any specific conclusions aside from the strong seasonality in the processes driving mixed layer DIC variations. Furthermore, no previous study has provided a large-scale view of Southern Ocean DIC fluxes based on year-round and circumpolar observations.

Recognizing the paucity of year-round biogeochemical data in the Southern Ocean, the SOCCOM project began deploying sea ice-enabled autonomous biogeochemical profiling floats in 2014. Since then, a new database has been growing that can be used to shed light on the carbon cycle in this hard-to-reach environment. In this study, we build a monthly mixed layer DIC budget using SOCCOM float data, complemented with atmospheric reanalysis. This framework allows us to investigate the processes that determine the seasonal cycle of carbon fluxes in different regions; namely, the Sea Ice Zone (SIZ) and Antarctic Southern Zone (ASZ), which are delimited by the Polar Front (PF) and winter sea ice edge (SIE) (Figure 1a). Section 2 covers the data sets used in this study. Section 3 elaborates on the budget framework, Section 4 presents the results on both annual and seasonal time scales, and Section 5 discusses the implications of our results.

2. Data Sets

2.1. Float Data

In this study, we use in situ data from the December 2020 snapshot of the SOCCOM Project data set (https://doi.org/10.6075/J0B27ST5). This snapshot covers the period from January 2014 to 22 December 2020 and contains data from 201 autonomous biogeochemical profiling floats. SOCCOM floats measure temperature (T), pressure (P) and salinity (S) over the top 2,000 m of the water column, every 10 days, similar to a typical Argo float. However, they also carry sensors for dissolved oxygen (O_2), nitrate, pH, chlorophyll fluorescence, and optical backscatter. Floats sample unevenly in the vertical, so all profiles are linearly interpolated onto a regular depth
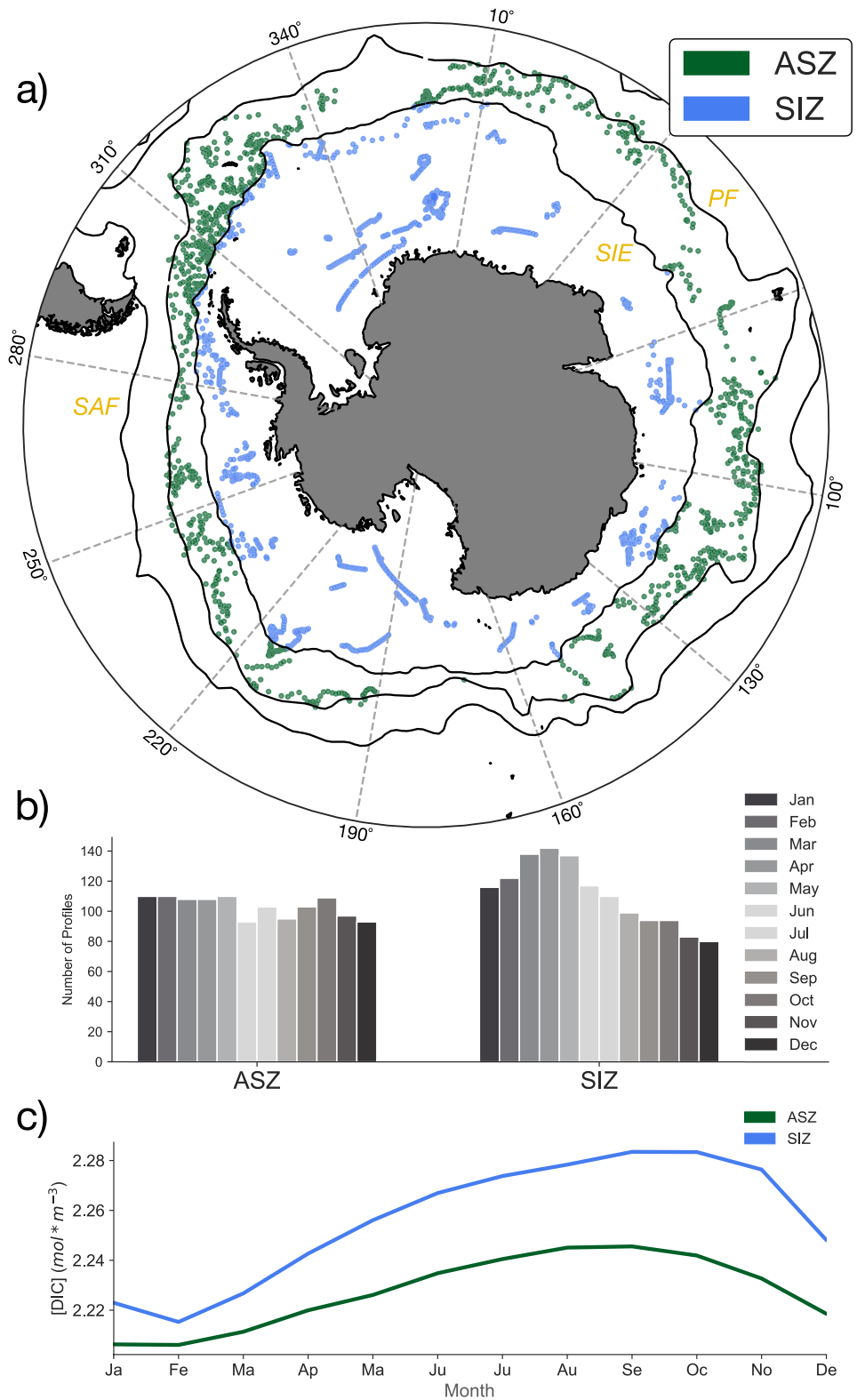
Figure 1. (a) Location of available float profiles with good pH data (i.e., where dissolved inorganic carbon (DIC) can be estimated), colored by zone (SIE: Sea Ice Edge, PF: Polar Front, SAF: Subantarctic Front). (b) Number of profiles available for analysis per month and per zonal region (c) Monthly and spatially averaged DIC concentration for the ASZ and SIZ (ASZ: Antarctic Southern Zone, SIZ: Sea Ice Zone).

axis with 5 m resolution in the upper 500 m, 10 m resolution from 500 to 1,000 m, 50 m resolution from 1,000 to 1,500 m, and 100 m resolution from 1,500 to 2,000 m. We only consider profiles with good pH data (i.e., where DIC content can be estimated), which leaves us with 7,029 profiles from 132 floats, reasonably well spatially distributed in the Southern Ocean (Figure 1a). We separate profiles according to the month and the zone (see Section 3.2) and obtain about 100 profiles per category (Figure 1b). We download a delayed-mode quality-controlled snapshot of the SOCCOM data (Maurer et al., 2021) and keep only the data flagged "Good" except for latitude and longitude, where we additionally keep under-ice data labeled "Questionable."

2.2. Ancillary Data

Monthly composites of the ERA5 reanalysis product, covering the period of January 2014 to December 2020, are used to create climatological seasonal cycles of eastward and northward wind stress, sea ice fraction, and evaporation and total precipitation rate (Hersbach et al., 2020). Monthly composites of the ORAS5 global ocean reanalysis product, also covering the period of January 2014 to December 2020, are used to create climatological seasonal cycles of eastward and northward sea ice velocity, sea ice fraction, and sea ice thickness (Zuo et al., 2019). Monthly fields from the Roemmich-Gilson Argo Climatology (RGAC) for the period of January 2014 to December 2020 are used to compute an average monthly climatology of potential temperature, which is used to estimate frontal positions (Roemmich & Gilson, 2009). A gridded product of geostrophic velocity updated from Gray and Riser (2014) with improved mapping and additional data points is used in the geostrophic transport calculations (see Section 3.3.3). Finally, we use the bathymetry from the ETOPO1 Global Relief Model (Amante & Eakins, 2009).

3. Budget Framework and Analysis Methods

In order to create a monthly climatology of the mixed layer budgets of carbon and oxygen, we use a box model framework with boxes defined by the Polar Front and the maximum sea ice extent. Thus, averaging over a region is roughly equivalent to applying a zonal average. Consequently, horizontal fluxes of carbon and oxygen need only be defined at the box's northern and southern edges (Figure 1a). Available float data are selected for a particular box (i.e., zonal region) and then averaged for each month, combining all available years to get a climatological seasonal cycle for each zone. We derive the mixed layer budget equation by volume integrating the tracer conservation equation for an arbitrary tracer, X, in this case DIC or O_2. The volume of the box can be converted to the product of the mixed layer depth (h) by the ocean surface area (A) of the box.

$$\iint_A \int_{-h(t)}^0 \left[\frac{\partial(\rho[X])}{\partial t} + \vec{u} \cdot \nabla(\rho[X]) = f_{air-sea} + \kappa_z \frac{\partial^2(\rho[X])}{\partial z^2} \right] dz dA \tag{1}$$

After solving and applying the appropriate assumptions, we obtain the final form of the budget equation (see Section 3.3 and Supporting Information S1 for details).

$$\frac{\partial(\rho[X]h)}{\partial t} = \rho[X]|_{-h} \frac{dh}{dt} - \frac{1}{A} \left[(\rho[X]V_{ek})|_N - (\rho[X]V_{ek})|_S + (\rho[X]V_{geo})|_N - (\rho[X]V_{geo})|_S \right]$$
$$+ w\rho[X]|_{-h} + F_{air-sea} - \kappa \frac{\partial(\rho[X])}{\partial z}\bigg|_{-h} + F_{bio} \tag{2}$$

In this form, we have canceled out the ocean surface area of the zonal region. However, multiplying any term by this area will return units of mol time^{-1}, which properly reflects the fact that our budget tracks the total quantity of DIC in the mixed layer over time. Each term of Equation 2 represents a different process that can cause an increase or decrease in tracer mixed layer molar concentration (mol m^{-3}). Equation 2 can be expressed in terms of the different fluxes at play, namely

$$\text{TEND} = F_{entrain} + F_{horiz-adv} + F_{vert-adv} + F_{air-sea} + F_{mixing} + F_{bio} \tag{3}$$

In Section 3.3, we give a detailed overview of each term and its derivation.

3.1. Initial Processing of the Float Data

We follow the method used by the SOCCOM project to determine DIC from the float data (Johnson et al., 2017; Wanninkhof et al., 2016). We estimate total alkalinity (TA) by using float-derived T, S, and O_2 as inputs to the LIAR algorithm (Carter et al., 2018). To estimate DIC, we use the CO_2 System Calculator for Python

(PyCO2SYS) which requires two carbonate system parameters, TA and in situ pH, as well as measured T, S, and P (Humphreys et al., 2021). We also provide total silicate and total phosphate concentrations estimated using stochiometric ratios of float-derived nitrate concentration. We use the equilibrium constant parameterizations of Lueker et al. (2000) to model carbonic acid dissociation, Dickson (1990) for bisulfate ion dissociation, Perez and Fraga (1987) for hydrogen fluoride dissociation, and Lee et al. (2010) for the boron:salinity relationship to estimate total borate.

We take the quality-controlled float data and average the relevant quantities in the mixed layer. To estimate the mixed layer depth (MLD), we find the absolute salinity and the conservative temperature using the Gibbs Sea-Water Oceanographic Toolbox for Python (McDougall & Barker, 2011). From those, we estimate the in-situ density (ρ) and the potential density anomaly with reference pressure of 0. We then interpolate the potential density anomaly to 0.01 dbar increments and use a density variation threshold of 0.03 kg m^{-3} from a reference pressure of 10 dbar from the surface to identify an approximate pressure for the base of the mixed layer (de Boyer Montégut et al., 2004; Holte & Talley, 2009). Note that the mixed layer pressure identified with this method includes the contribution of any sea ice present at the surface of the water column.

We select profiles which have at least one value in the top 30 dbar and at least two values in the top 1,000 dbar, though only 1% of the DIC profiles have less than 50 data points. We fit a curve to each profile using a Piecewise Cubic Hermite Interpolating Polynomials (pchip) interpolator as they have been shown to be more accurate than linear interpolation schemes at representing the curvature found in vertical profiles of oceanographic data (Y. Li et al., 2022). We then find the average concentration in the mixed layer. This averaging is executed for the biogeochemical tracers' molality (concentration of tracer in mol kg^{-1} of seawater) multiplied by ρ to obtain the average mixed layer molar concentration of each variable (mol m^{-3}, called concentration for the remainder of this study). We also find the vertical gradient below the mixed layer by fitting a straight line through the data between the mixed layer pressure and 20 dbar deeper, finding its slope and converting to depth units by multiplying by $-g\rho 10^{-4}$. We then average the float data monthly and by zonal region, multiplying by h beforehand as the budget equation requires.

3.2. Zonal Regions

We sort profiles into two different zones, shaped like concentric circles around the continent of Antarctica (Figure 1a) based on the Polar Front (PF), the sea ice edge (SIE) and the 1,000 m isobath. The sea ice zone (SIZ) is defined as the region south of the SIE where waters are at least 1,000 m deep. The Antarctic Southern zone (ASZ) can be found north of the SIE and south of the PF. This is similar to a number of previous papers (Bushinsky et al., 2019; Gray et al., 2018). We define the PF using the 2°C contour at the minimum potential temperature of the top 200 m. We compute the position of the front at monthly resolution by applying the Orsi et al. (1995) criteria to the RGAC monthly climatology of potential temperature (Figure S1 in Supporting Information S1). We use the 15% sea ice concentration contour in September to identify the Sea Ice Edge (SIE).

3.3. Budget Terms

The following section will provide details about the different terms of the mixed layer budget and their derivation.

3.3.1. Tendency and Entrainment Flux

The left-hand side, or tendency (TEND), of Equation 2 corresponds to the time rate of change of the tracer concentration (mol m^{-3}) in the box. The entrainment flux is due to the processes by which the base of the mixed layer deepens or shoals. During mixed layer deepening, water below the mixed layer is integrated into the surface layer leading to mixed layer volume and tracer content increasing, proportionally to the amount of tracer in the waters just below the base of the mixed layer. During mixed layer shoaling, mixed layer volume decreases and so does the amount of tracer in the mixed layer, proportionally to the mixed layer concentration. Both the TEND and $F_{entrain}$ can be estimated from float-derived molality, the thickness of the mixed layer (h) and ρ, using a centered difference calculation. Integrating the first component of Equation 1 over a time-varying $h(t)$ produces two terms, the tendency term (the rate of change of the total tracer amount) and the entrainment term (proportional to the rate of change of the MLD) (see Supporting Information S1 for details). The tendency term is given by

$$\text{TEND} = \frac{\partial(\rho[X]h)}{\partial t} \tag{4}$$

and the entrainment term is expressed as

$$F_{entrain} = \rho_{-h}[X]_{-h}\frac{dh}{dt} \ \text{ if } \frac{dh}{dt} > 0 \tag{5}$$

$$F_{entrain} = \rho[X]\frac{dh}{dt} \ \text{ if } \frac{dh}{dt} < 0 \tag{6}$$

both terms having been divided by the area to be consistent with Equation 3.

It is important to note that the subtraction of the entrainment flux from the tendency is equivalent to the rate of change of the concentration multiplied by the mixed layer depth (h). This will be used in the presentation of the results.

$$\frac{\partial(\rho[X]h)}{\partial t} - (\rho[X])_{-h}\frac{dh}{dt} = h\frac{\partial(\rho[X])}{\partial t} \tag{7}$$

3.3.2. Air-Sea Flux

We estimate the air-sea fluxes of carbon using the method from Gray et al. (2018). Using float-measured pH and a float-based estimate of alkalinity, we compute $p\text{CO}_2$ at the surface of the ocean. We then use monthly observations of the mole fraction of CO_2 in dry air from air samples at the Cape Grim Observatory in Tasmania which we interpolate to a 6-hourly timescale. To derive atmospheric $p\text{CO}_2$, we combine these measurements with estimates of the mean sea level pressure at each profile location, corrected for water vapor pressure using the method of Zeebe and Wolf-Gladrow (2001). The air-sea flux of carbon can then be estimated using the following equation, where k_g is the gas transfer velocity and K_0 is the solubility of CO_2:

$$f_{air-sea} = k_g K_0 \left(p\text{CO}_2^{ocn} - p\text{CO}_2^{atm}\right). \tag{8}$$

We use a squared wind speed-dependent parameterization to compute k_g from the Schmidt number and an estimate of the 10-m wind speed (Wanninkhof, 2014). Because carbon dioxide is highly soluble in seawater, we do not need to account for the effect of bubble fluxes. If sea ice is present at the surface, we find the sea ice concentration (C_{si}) at a particular profile location from satellite observations. We then apply a correction factor of $(1-C_{si})$ to the flux value. If $C_{si} > 95\%$, we set C_{si} equal to 95% to account for the presence of leads in sea ice.

We estimate the oxygen air-sea fluxes following Bushinsky et al. (2017). Contrarily to carbon, oxygen is a relatively insoluble gas, and bubble fluxes must be taken into account. The total air-sea flux is thus made up of three components: F_s is the diffusive component, F_c accounts for small bubbles that collapse while under water, and F_p accounts for big bubbles that partly escape the water column. β is the tuning parameter.

$$f_{air-sea} = F_s + \beta F_c + \beta F_p \tag{9}$$

To obtain the form of the air-sea flux that is consistent with Equation 3 ($F_{air-sea}$), we compute the air-sea flux ($f_{air-sea}$) at high frequency (6-hourly) and then find the average air-sea flux of tracer per meter squared (mol m^{-2} day^{-1}) for each zonal region.

3.3.3. Advective Flux

The advective fluxes originate from the second term of Equation 1, which we separate into a horizontal and a vertical component. We consider the horizontal advection crossing the zonal boundaries at the northern and southern edges of the box only. In the Southern Ocean, cross-front (largely meridional) advection at the surface is mostly due to Ekman transport, which is northward due to the strong westerly winds. Additional contributions to the cross-front advection come from the geostrophic flow, which can be decomposed into low-frequency (mean and seasonal cycle) and high-frequency (eddying) components. In the context of this work, we neglect the cross-front advection due to eddies because it has been shown to be more than 50% smaller than the time mean component in the Ekman layer (Dufour et al., 2015). Defining V_{ek} and V_{geo} as the Ekman and geostrophic mass transports, the final form of the horizontal advection term equation, as consistent with Equation 3, becomes

$$F_{horiz-adv} = -\frac{1}{A}\left[(\rho[X]V_{ek})|_N - (\rho[X]V_{ek})|_S + (\rho[X]V_{geo})|_N - (\rho[X]V_{geo})|_S\right] \tag{10}$$

(see Supporting Information S1 for details). Here, $\rho[X]|_N$ ($\rho[X]|_S$) corresponds to the tracer concentration of the source water of the horizontal advection at the northern (southern) boundary. This will change depending on the direction of mass flux (northward or southward). For example, Ekman transport in this region is northward. Consequently, we multiply the Ekman mass transport at the northern (southern) boundary of the zone by the concentration of tracer in (just South of) the zonal region (Figure S4 in Supporting Information S1).

We can compute the Ekman mass transport (V_{ek}) using ERA5 wind stress data. We take the monthly averaged wind stress and interpolate the data to each (latitude, longitude) point defining the boundaries of the zones. Using both the zonal and the meridional wind stress, we compute the component of the wind stress parallel to each segment of the boundary, defined by two (latitude, longitude) points. Taking the along-boundary wind stress, we convert it to the depth integrated Ekman velocity across the boundary using the Coriolis equation (Equation S10 in Supporting Information S1). Integrating further zonally around the boundary, we obtain the Ekman transport across the boundary of the zone (m^3 time^{-1}) (See Appendix A1).

The geostrophic mass transport is computed using an updated version of the geostrophic velocity product from Gray and Riser (2014). Similarly to the process for Ekman transport, the data is interpolated to boundary locations and the across-boundary geostrophic velocity is identified at each segment of the boundaries of the zones. This geostrophic velocity is then integrated zonally along the boundary before being integrated further in depth to the mixed layer depth of the zone being considered (See Appendix A1).

The vertical advection at the base of the mixed layer depends on the vertical velocity at the base of the mixed layer (w_{-h}) as well as on the concentration of tracer ($\rho[X]|_{-h}$) in the downwelled or upwelled waters depending on the sign of w_{-h}.

$$F_{vert-adv} = (w\rho[X])|_{-h} \tag{11}$$

Vertical velocity is more challenging to determine from satellite products as it is comparatively small. We use a mixed layer mass budget to determine the monthly mean vertical velocity averaged across each zone. The equation for the mixed layer mass budget is determined by integrating the advection-diffusion equation for density over the mixed layer volume in a process similar to the derivation for the tracer conservation equation. The resulting equation has many of the same terms as the biogeochemical budget equation.

$$\frac{d(A\rho h)}{dt} = F_{entrain} + F_{surface} + F_{horiz-adv} + F_{vert-adv} \tag{12}$$

The rate of change with time of the mass of water in the mixed layer as well as the entrainment flux of water can both be determined from float-derived data following Equation 7 applied to the density (kg m^{-3}) instead of the concentration of tracer (mol m^{-3}). Similarly, the horizontal mass advection can be determined following Equation 10. We use ERA5 precipitation, evaporation, and sea ice concentration data to estimate surface fluxes of mass ($F_{surface}$). For the sea ice contribution, we take the centered difference of the sea ice area combined with an estimated seasonal sea ice thickness (H. Li et al., 2018) to find the rate of change with time of the sea ice volume for each month. We use ORAS5 sea ice velocity and sea ice thickness to estimate the sea ice transport across each zonal boundary with the same method as for the Ekman and geostrophic transports. We subtract the volume of sea ice advected into the zone from the rate of change of the sea ice volume to get the sea ice contribution to the surface mass flux. Since the mass budget doesn't have biological fluxes or fluxes due to mixing, there is only one unknown, w_{-h}, which we solve for (Figure S3 in Supporting Information S1) (See Appendix A2).

3.3.4. Mixing Flux

Vertical mixing represents multiple processes involving the gradient of tracer concentration between the mixed layer and the waters underlying it. It differs from vertical advection because there is no exchange of mass. It is typically parameterized in terms of a vertical eddy diffusivity (κ_z), which ideally is tuned to observations. The mixing flux term corresponds to the last term of Equation 1,

$$F_{mixing} = -\kappa_z \left. \frac{\partial(\rho[X])}{\partial z} \right|_{-h} \tag{13}$$

(see Supporting Information S1 for details). There are very few observations of the vertical eddy diffusivity in the Southern Ocean and few observations at the base of the mixed layer. Law et al. (2003) estimate that the mean

effective vertical diffusivity is less than 0.3×10^{-4} m^2 s^{-1} in the Antarctic Circumpolar Current (ACC) region (61°S, 140°E) using a tracer dispersion experiment. Cronin et al. (2015) used data from moorings, satellites, and Argo floats to construct mixed layer budgets of heat and salt and estimate the residual diffusive flux of heat or salt across the base of the mixed layer. This residual flux implies a vertical eddy diffusivity of 1–3×10^{-4} m^2 s^{-1} in summer and spring for an open ocean location in the Northeast Pacific subpolar gyre. Please refer to Section 3.4 for details on how we estimate this parameter for the budgets presented here.

3.3.5. Biological Flux

The net contribution of all biological activity to changes in the concentration of tracer in the mixed layer of each zone is represented by the biological flux term (F_{bio}). Also included in this quantity are any non-explicitly represented physical processes. In the following section, we detail the method used to estimate both this term and the unknown eddy diffusivity parameter necessary for the mixing flux.

3.4. Optimization of the Coupled DIC and O$_2$ Budgets

To find the few parameters that cannot be easily estimated from float or reanalysis data, we define, for each zonal region, a system of 24 non-linear coupled equations (the monthly equations for the DIC and O$_2$ budgets) with 14 unknowns, where Y_X represents all terms that can be estimated from float or reanalysis data.

$$Y_{DIC} = -\kappa_z \left. \frac{\partial \rho[C]}{dz} \right|_{-h} + F_{biology-DIC} \tag{14}$$

$$Y_{O_2} = -\kappa_z \left. \frac{\partial \rho[O_2]}{dz} \right|_{-h} + R_{O_2/C} F_{biology-DIC} \tag{15}$$

We assume a single value of eddy diffusivity (κ_z) for all months in a zonal region. We use the respiration quotient $\left(R_{O_2/C} \right)$ to link the biological flux of DIC and O$_2$ and assume that this ratio doesn't change from month to month in a particular zone. This leaves us with 12 monthly carbon biological fluxes, one value of κ_z and one value of $R_{O_2/C}$ as the unknowns for each region. Using our system of equations, we construct a cost function that we minimize to determine the missing parameters. We use the Trust Region Reflective algorithm as part of a non-linear problem solver, to which we provide a Jacobian, to find a local minimum of our cost function (Branch et al., 1999) (See Appendix A3).

3.5. Uncertainty Estimation

Unlike model budgets which can be closed exactly, our budget framework is based on several observational products, which each have their own uncertainties. Furthermore, we have used an optimization method to find the value of some parameters. As such, the budget has a non-zero residual (Figures S8 and S9 in Supporting Information S1). The residual is small compared to the other monthly carbon fluxes (about 1%–2% of the average value of the flux for each month, except February and September in the SIZ where the fluxes are small and the residual is proportionally bigger), which gives us more confidence in our results. We also estimate an uncertainty for each monthly budget term.

To estimate the uncertainty associated with the results of the mixed layer budgets, we use a Monte Carlo simulation with 1,500 iterations. The uncertainty and degree of correlation of each data variable used in the simulation can be found in Table A1 (See Appendix A4). The uncertainty associated with each budget result is set to one standard deviation of the mean of the 1,500 simulations. We use a uniform distribution for the error in T, S, P and a normal distribution for all other variables. To estimate the uncertainty on the monthly composite of wind stress from ERA5, we interpolate the x- and y-direction wind stress at each boundary location for each ensemble member available from ERA5. We set the uncertainty as one standard deviation from the mean of the ensemble members. Similarly for the sea ice fraction from ERA5, we set the uncertainty of the change in sea ice fraction over a month as one standard deviation from the mean of the ensemble members. We use the uncertainty estimates provided by the LIAR algorithm for the uncertainty in TA (Carter et al., 2018). We set the uncertainty of the geostrophic velocity interpolated at each (latitude, longitude) location of the zone boundaries to be 20% of the velocity, which is a conservative estimate based on the methodology (Gray & Riser, 2014). We also set the uncertainty of the sea ice transport and the sea ice thickness to be 20% since sea ice thickness estimates tend

to vary depending on which product is used (see Kern and Spreen (2015) e.g.). The uncertainty on the air-sea fluxes of carbon and oxygen was estimated separately following the methods of Gray et al. (2018) and Bushinsky et al. (2017), then used in the Monte Carlo.

Among the 1,500 iterations of the Monte Carlo simulation, 15% (16%) of the eddy diffusivities (or κ_z) identified by the optimization scheme are negative for the ASZ (SIZ). This indicates up-gradient eddy diffusion of carbon which is not expected. However, when taking all iterations together, the averaged value of κ_z does converge to a positive value of the expected magnitude, as is also the case when running the budget with no uncertainty added. The presence of negative κ_z values points toward the fact that this system is physically fragile and may flip to a different, maybe non physically realistic, state easily. This fragility probably originates from the identification of the MLD, which is sensitive to the addition of uncertainties to the temperature and salinity profiles.

The budget framework assumes that the biological processes taking up or releasing DIC in the mixed layer are only photosynthesis and respiration. However, formation and dissolution of calcium carbonate by certain phytoplankton species also change the mixed layer DIC and alkalinity content while not influencing the oxygen content (Krumhardt et al., 2020). This process is not accounted for in our budget, which is a reasonable assumption for the ASZ and SIZ where there is low abundance of calcifying organisms (Balch et al., 2016) and the mixed layer DIC consumption attributed to particulate inorganic carbon production, like calcium carbonate, is relatively low compared to organic carbon production (Huang et al., 2023).

In this study, DIC concentration is calculated from in situ pH and empirically estimated alkalinity. Most of the uncertainty in the DIC concentration arises from the uncertainty in TA provided by the LIAR algorithm, which is defined for each depth and latitude-longitude position. We then propagate this uncertainty through the Monte Carlo simulation, assuming that the uncertainty is random to avoid introducing spurious variability in our results. We should note, however, that the TA uncertainty may be correlated in time, at least seasonally. Testing the algorithm against seasonally resolved measurements would be required to determine how much of the uncertainty is correlated in time. As such, the uncertainty on the DIC fluxes may be underestimated here.

4. Results

4.1. Drivers of the Annual-Mean Mixed Layer Carbon Budget

We first consider the drivers of the annually integrated air-sea flux of carbon in the high-latitude Southern Ocean (Figure 2a). Note that the tendency term of Equation 3 integrates to 0 by definition and does not appear in the annually integrated results. We find a net outgassing of carbon in both zones. In the ASZ, the outgassed carbon enters the mixed layer by mixing with carbon-rich waters from the interior. This mixing flux comprises eddy-driven processes that can transfer DIC across the mixed layer base without any exchange of fluid. The DIC mixed in from below is then either consumed by net community production or outgassed to the atmosphere. The magnitudes of the annual advective and entrainment fluxes are small. In the SIZ, the annual fluxes of DIC are of smaller magnitude in general than those in the ASZ. Similarly to the more northerly region, the annually averaged contribution from the entrainment flux is small, and DIC principally enters the mixed layer due to mixing from below. However, since the outgassing signal and the annual biological flux are weaker, the surplus of carbon is carried north to the ASZ by net Ekman transport.

This flux of DIC from the SIZ supports an outgassing signal in the ASZ by providing an additional source of carbon to the mixed layer. Since the magnitudes of the individual advective fluxes are so much greater than the net DIC advection (Figure 2b), small changes in the individual components of the advective flux could significantly alter the sign and magnitude of the net advective flux. For example, if sea ice retreats under climate change, it could decrease the capping effect of sea ice in the SIZ which is currently acting to prevent carbon outgassing in winter. This could lead to a decrease in the flux of DIC to the ASZ and the location of CO_2 outgassing could move south into the SIZ. In this way, changes in the transport at the southern boundary of the ASZ may be critical in determining the net air-sea flux of carbon dioxide in this region.

### 4.2. Seasonally-Varying Fluxes of Carbon in the Mixed Layer

The monthly averaged fluxes reveal similar seasonal patterns in air-sea carbon flux across both high-latitude regions, with carbon uptake by the ocean in summer partly opposing carbon outgassing during the rest of the year (Figures 3 and 4). In the ASZ, the air-sea flux is stronger and peaks at the end of winter (September), while
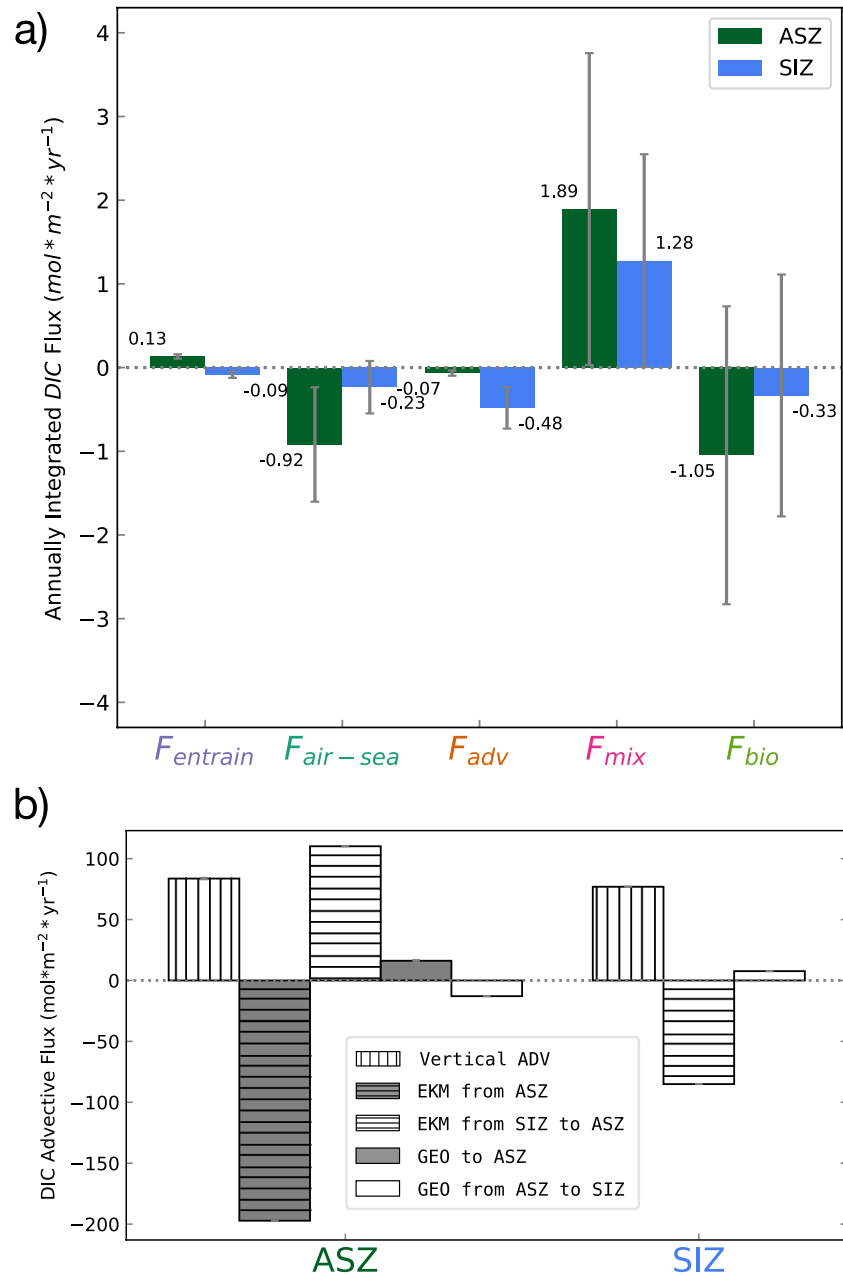
Figure 2. (a) Annually integrated fluxes of dissolved inorganic carbon (DIC) and their uncertainty indicated by the gray bars. Negative values indicate that DIC is being removed from the mixed layer of the zone in question ($F_{entrain}$: Entrainment flux, $F_{air-sea}$: Air-sea flux, F_{adv}: Advective flux, F_{mix}: Mixing flux, F_{bio}: Biological flux) (b) Annually integrated advective fluxes of DIC which add up to F_{adv} from panel a (uncertainty is not shown because error bars are too small). "EKM from SIZ to ASZ" is the northward Ekman transport of DIC across the boundary separating the SIZ and the ASZ. Since the budget is computed per m², this term has a different magnitude when considered for the SIZ or the ASZ as the area of the zones are different (Vertical ADV: vertical advection of DIC, EKM from ASZ: Ekman advection of DIC from the ASZ northward to the PFZ, EKM from SIZ to ASZ: Ekman advection of DIC from the SIZ northward to the ASZ, GEO to ASZ: geostrophic advection of DIC southward from the PFZ to the ASZ, GEO from ASZ to SIZ: geostrophic advection of DIC southward from the ASZ to the SIZ) (PFZ: Polar Frontal Zone, ASZ: Antarctic Southern Zone, SIZ: Sea Ice Zone).

in the SIZ carbon outgassing is strongly modulated by sea ice concentration and peaks in May (Butterworth & Miller, 2016).

We find that the seasonal variations in carbon air-sea flux lag one to 2 months behind the contribution from the term obtained by subtracting the entrainment from the tendency term (TEND$-F_{entrain}$, Figures 3a and 4a). This
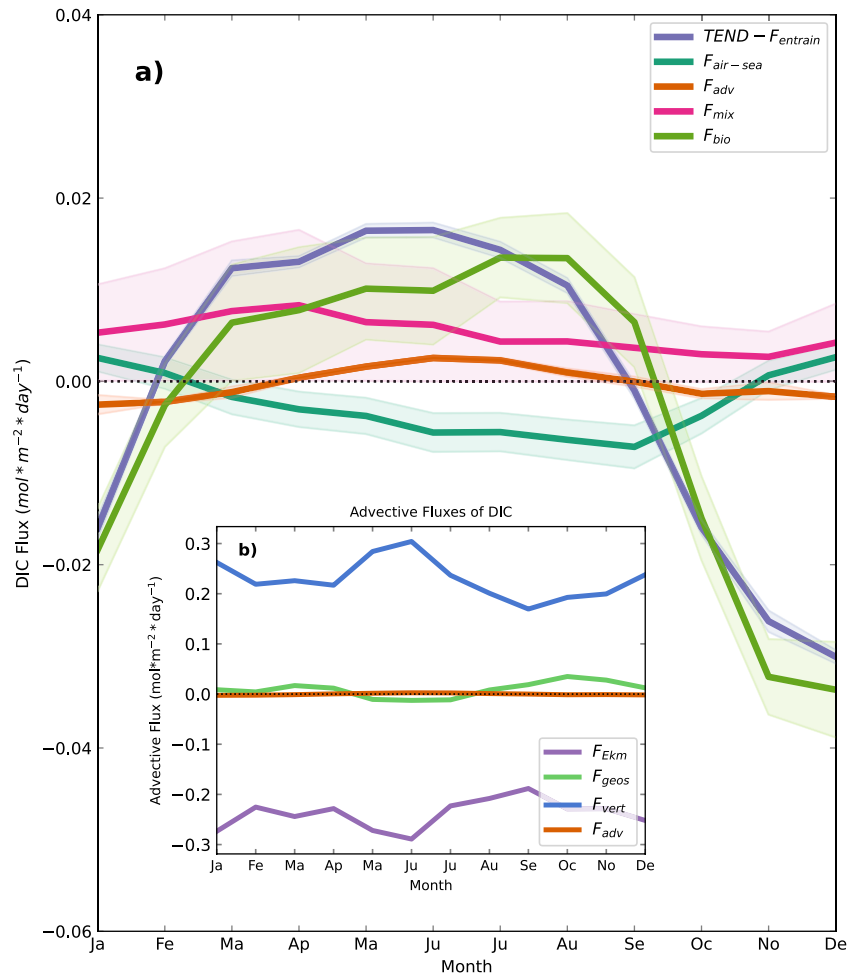
Figure 3. Monthly averaged fluxes of dissolved inorganic carbon (DIC) to and from the ASZ mixed layer. (a) DIC fluxes are presented with their uncertainty of one standard deviation (TEND: Tendency, $F_{entrain}$: Entrainment flux, $F_{air-sea}$: Air-sea flux, F_{adv}: Advective flux, F_{mix}: Mixing flux, F_{bio}: Biological flux) (b) The components of the advective flux are presented: the flux of DIC due to Ekman advection (F_{Ekm}), geostrophic advection (F_{geos}), vertical advection (F_{vert}), as well as the net advective flux of DIC (F_{adv}). Uncertainty on the components of the advective flux is very small. Negative (positive) fluxes remove (add) carbon from (to) the mixed layer. (ASZ: Antarctic Southern Zone).

relationship is confirmed by a strong anticorrelation of −0.93 (−0.87) or −0.88 (−0.83) at 1 or 2 months lag for the ASZ (SIZ). The TEND−$F_{entrain}$ term is equivalent to the time rate of change of the mixed layer concentration multiplied by the mixed layer depth (see Equation 7). Both the TEND and $F_{entrain}$ are two orders of magnitude larger than the other fluxes (not shown). However, their net effect is much smaller and comparable to the other processes that change the mixed layer DIC. Since the seasonal cycle in mixed layer depth is only weakly correlated to the seasonal cycle in TEND−$F_{entrain}$ (0.39 and 0.45 for the ASZ and SIZ respectively, Figure S2 in Supporting Information S1), we interpret seasonal variations in TEND−$F_{entrain}$ to be caused by variations in the rate of change of mixed layer DIC concentration. Periods of carbon outgassing (uptake) tend to follow periods of concentration increase (decrease) by about 1 month, suggesting that changes in mixed layer DIC concentration are driving the air-sea fluxes of carbon in the zonal regions under study (Gruber et al., 2019). To support the link between carbon air-sea fluxes and surface DIC concentration, we examine the drivers of pCO$_2$ seasonal variability by computing pCO$_2$ in pyCO2SYS while varying only one variable at a time. We find that in the high-latitude Southern Ocean, nearly all variability is due to seasonal changes in pH and thus to changes in DIC (Figure S17 in Supporting Information S1).

Seasonal variations in the mixed layer DIC concentration change are driven chiefly by changes in the biological flux term in both zones (Figures 3a and 4a), as confirmed by a strong correlation of 0.97 and 0.95 at no lag for
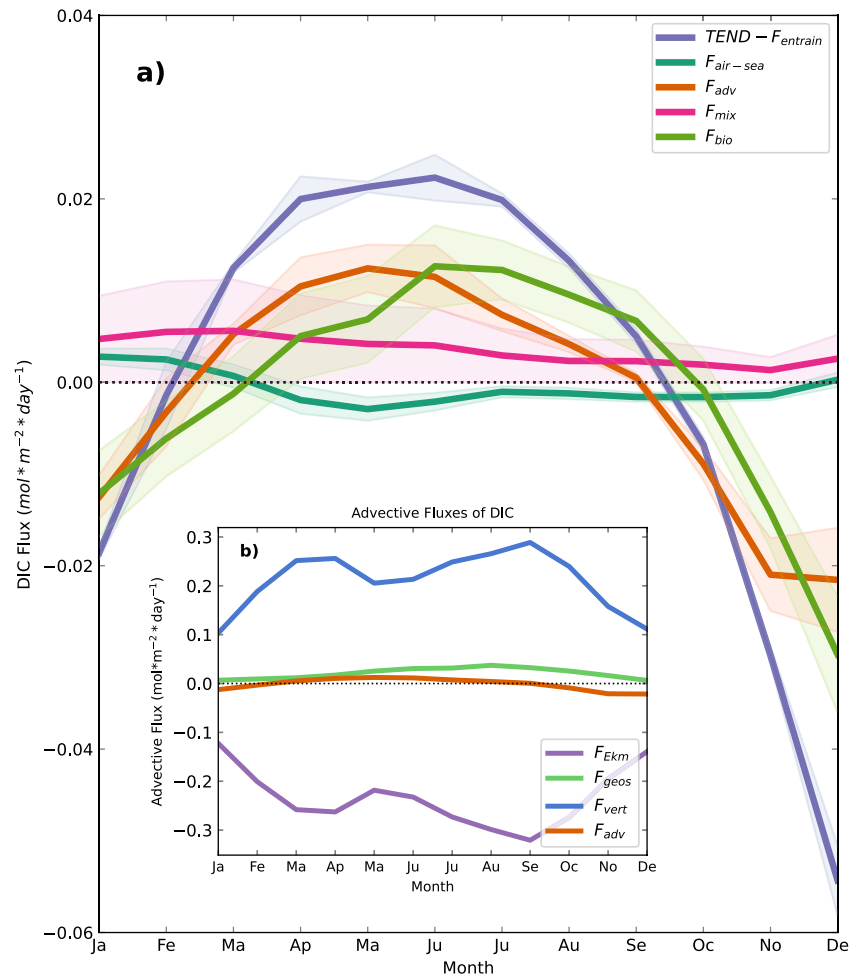
Figure 4. Monthly averaged fluxes of dissolved inorganic carbon (DIC) to and from the SIZ mixed layer. (a) DIC fluxes are presented with their uncertainty of one standard deviation (TEND: Tendency, $F_{entrain}$: Entrainment flux, $F_{air-sea}$: Air-sea flux, F_{adv}: Advective flux, F_{mix}: Mixing flux, F_{bio}: Biological flux) (b) The components of the advective flux are presented: the flux of DIC due to Ekman advection (F_{Ekm}), geostrophic advection (F_{geos}), vertical advection (F_{vert}), as well as the net advective flux of DIC (F_{adv}). Uncertainty on the components of the advective flux is very small. Negative (positive) fluxes remove (add) carbon from (to) the mixed layer. (SIZ: Sea Ice Zone).

the ASZ and SIZ, respectively. Biological activity adds carbon to the mixed layer when DIC concentration is increasing, probably due to net respiration, and the biological flux removes carbon from the mixed layer during the spring and summer phytoplankton bloom. The strength of this bloom is greater in the ASZ, as can be seen by the strong drop in the biological flux between September and November. In the SIZ, the seasonal cycle of the advective flux (Figure 4a) is just as important as variations in the biological flux in driving changes in mixed layer DIC concentration (correlation of 0.97 at no lag).

The net advective flux is the sum of the Ekman, vertical and geostrophic components (Figure 4b). We assume that the contribution from eddy-driven advection is small in the mixed layer for the timescales considered here. The individual advective components dominate over the other DIC fluxes (Figures S13 and S14 in Supporting Information S1), but the Ekman and vertical components largely compensate so that the net advection is of smaller magnitude. We find a net positive advective flux of DIC in fall and winter, indicating a dominance of vertical advection over the net meridional advection, while the opposite occurs in summer and spring. In the ASZ, the magnitude of the advective flux is much smaller than the biological flux (Figure 3a), though we do observe a sign reversal similar to the SIZ, from net positive flux in winter to net negative flux in summer. In both zones, the flux of DIC from diffusive mixing with carbon-rich waters at the mixed layer base always acts to bring DIC into the mixed layer (Figures 3a and 4a). In both regions, the seasonal variations of the mixing flux are not strongly correlated with the change in DIC concentration.
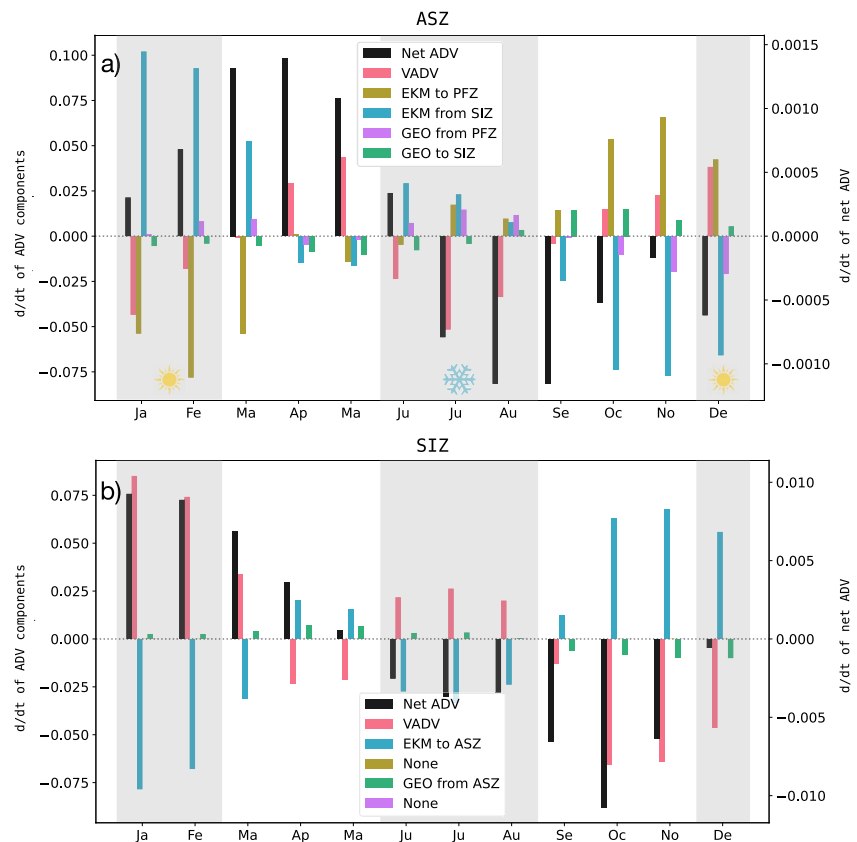
Figure 5. First time-derivative of the monthly averaged advective fluxes of dissolved inorganic carbon (DIC) for (a) the ASZ and (b) the SIZ (mol m^{-2} day^{-1} month^{-1}). Note that the net advective flux (Net ADV) is plotted on its own axis (right) and the components of the net advective flux (Ekman (EKM), geostrophic (GEO) and vertical (VADV) advective fluxes of DIC) are plotted on the left axis. The gray shading indicates the summer and winter months. (PFZ: Polar Frontal Zone, ASZ: Antarctic Southern Zone, SIZ: Sea Ice Zone).

In both zones, seasonal variations in the net advective flux of DIC can be attributed to a combination of changes in the Ekman flux of DIC from the SIZ to the ASZ and changes in the vertical advection signal, though the months where one or the other dominates are not the same across the study region (Figure 5).Changes in the southward geostrophic transport of DIC are also correlated with changes in the net advection, but the magnitude of the geostrophic advection is one order of magnitude smaller than the Ekman and vertical advections (Figures S13 and S14 in Supporting Information S1).

By comparing the period of carbon outgassing (April to August) to the period of carbon uptake (December to January), we gain further insight into what drives the seasonal fluxes in this region. During wintertime outgassing, the mixed layer DIC concentration is increasing (positive value of TEND$-F_{entrain}$, Figures 3a and 4a) because net respiration, eddy-driven mixing from below, and net vertical advection bring DIC into the mixed layer. Some of this DIC is then outgassed to the atmosphere (Figures 3a and 4a). During the summer period of oceanic carbon uptake, the mixed layer DIC concentration is decreasing due to strong net photosynthesis and a net Ekman northward advection of DIC. This superposition of processes leads to carbon uptake from the atmosphere (Figures 3a and 4a). However, mixing with carbon-rich waters below is still bringing DIC into the mixed layer, which may contribute to the observed net outgassing signal over a full seasonal cycle.

The shift from carbon outgassing to uptake corresponds to a shift from respiration to photosynthesis and from net positive to net negative advection (Figures 3a and 4a). In the ASZ, the net advective flux of DIC primarily changes sign because of transport at the southern boundary; namely, Ekman advection of DIC from the SIZ (Figure S13 in Supporting Information S1) decreases significantly from winter to summer (by 53% on average), while the vertical advective flux and Ekman transport at the northern boundary stay relatively constant (decreases

by 15% and 28% respectively). In the SIZ, most components of the advective flux decrease by approximately half during months of carbon uptake compared to months of outgassing (Figure S14 in Supporting Information S1).

The seasonal change in the Ekman advective flux of DIC at the sea ice edge is due to changes in Ekman mass transport driven by wind variations, rather than changes in the DIC concentration of the SIZ. We observe that the seasonal cycle in the Ekman mass advection and its components is very similar to that of the Ekman DIC advection (Figures S13 to S16 in Supporting Information S1). Furthermore, the amplitude of seasonal variations of the Ekman mass advection at the SIE is 74% (83%) for the ASZ (SIZ) which compares well to the amplitude of seasonal change of the Ekman DIC advection at the SIE (76% (85%) for the ASZ (SIZ)), while the amplitude of seasonal variations in the mixed layer DIC concentration of the SIZ used to convert mass transport to DIC advection is only 3% in both zones.

5. Discussion

The Southern Ocean is an essential part of the global climate system because of its important contribution to the total oceanic uptake of anthropogenic carbon. However, the uncertainty of the ocean carbon sink is highest in the Southern Ocean (Fay & McKinley, 2021; Friedlingstein et al., 2022; Gloege et al., 2021) and the discrepancy between models and observations is also most significant there compared to other ocean basins (Hauck et al., 2020). There is also discrepancy between observational estimates of the Southern Ocean carbon sink, or the carbonate parameters necessary to determine it, based on the method or data set used (Bushinsky & Cerovečki, 2023; Coggins et al., 2023; Long et al., 2021; Mackay & Watson, 2021; Wu et al., 2022; Wu & Qi, 2022). Further, sampling alias linked to the spatial distribution of available observations has been shown to be significant (Hauck et al., 2023). For this reason, it is essential to better understand the processes driving surface ocean $p\text{CO}_2$, and thus the air-sea carbon flux, in order to improve the representation of the Southern Ocean carbon sink in models. The mixed layer budget presented in this study provides a useful framework for understanding the relative roles of the mechanisms that drive air-sea carbon fluxes at seasonal and annual timescales in the high-latitude Southern Ocean.

Using a monthly mean climatology of the mixed layer carbon budget, we show that small-scale mixing at the base of the mixed layer provides DIC to the surface layer year-round. In the ASZ, most of this DIC is then consumed by net biological production, while the net biological flux is weaker in the SIZ. On an annual timescale, the surplus of DIC in the mixed layer from the balance of these two processes is either advected from the SIZ to the ASZ by Ekman divergence or outgassed to the atmosphere in the ASZ. Physical transport of carbon, in concert with the transition from net production to net respiration, also explains the difference between seasonal periods of carbon outgassing (fall to spring) and uptake (summer).

Values for the vertical eddy diffusivity at the base of the mixed layer are sparse in the literature. Still, the magnitude of the diffusivity obtained from our optimization scheme (between 2.95 and 6.83 $\times$ 10^{-5} m^2/s) is similar to the only comparable published value in the Southern Ocean (less than 3 $\times$ 10^{-5} m^2/s) (Law et al., 2003). The ASZ makes up the southern part of the ACC, where wind-driven upwelling brings carbon-rich isopycnals to the near-surface. The high-latitude Southern Ocean also exhibits strong vertical DIC gradients (Dove et al., 2022); therefore, it is not surprising that subsurface mixing plays a strong role in supplying DIC to the mixed layer. In the SIZ, there is also upwelling of carbon-rich deep waters. However, the SIZ is characterized by multiple gyre circulations as well as sea ice cover, which can act to isolate the surface ocean from the atmosphere and may be a barrier to momentum transfer (Shadwick et al., 2021; Vihma & Haapala, 2009). Indeed, we find a stronger mixing flux of DIC in the ASZ compared to the SIZ due to differences in the eddy diffusivity (see Section A3 in Appendix A), consistent with more wind energy input in the ASZ resulting from stronger winds and lack of ice cover. However, the vertical gradient of DIC near the base of the mixed layer is stronger in the SIZ, most probably due to gyre dynamics allowing respired DIC to accumulate in the surface waters (MacGilchrist et al., 2019).

We find that inorganic carbon entering the mixed layer through eddy processes is mostly consumed by biological production. This is similar to previous results by Hauck et al. (2013), who found that biological processes remove more DIC from the mixed layer than air-sea fluxes. In the ASZ specifically, net production is the dominant sink of DIC in the mixed layer at annual timescales. We find annual net production of 1.05 mol C m^{-2} yr^{-1} in this region, consistent with previous float-based annual net community production estimates at similar latitudes (about 1–2 mol C m^{-2} yr^{-1}) (Arteaga et al., 2019). In the SIZ, we also find annual net production, which agrees

with model-based results (Carroll et al., 2022). Note though that, in both zones, error bars are large and extend to a value of net respiration. This agrees with the analysis of Briggs et al. (2018) who found that respiration in winter nearly balanced out biological production. Still, in both zones, we find an important net production signal in spring and summer and that the DIC tendency typically follows the biological flux, as has been reported in past studies (Carroll et al., 2022; Munro et al., 2015; Williams et al., 2018; Yang et al., 2021). In winter in both zones, we find net respiration of the same order of magnitude as the seasonal photosynthesis signal, due to low light availability (even more significant for the SIZ).

In the SIZ, the role of DIC advection is as important as the biological flux in both the seasonal and annual budgets. In the annual view, a large fraction of the surplus of DIC from subsurface mixing is advected to the ASZ by the Ekman transport component, with the rest either consumed by the net biological flux or outgassed. This is likely due, in part, to the wintertime ice cover preventing (or limiting) outgassing, as the surface ocean $p\mathrm{CO_2}$ values alone imply a stronger outgassing than is observed. Indeed, a sea ice capping effect has been reported on the continental shelf (Shadwick et al., 2021) and in idealized models (Gupta et al., 2020). Still, without physical transport removing available DIC from the region in winter, there would be less potential for carbon uptake in summer after the sea ice melts. As such, seasonal variability in the net advective flux is important for explaining the low annual outgassing signal in the SIZ. Throughout the year, vertical advection supplies carbon to the mixed layer, while horizontal advection (dominated by Ekman divergence) removes DIC from the region. Net advection is the smaller residual of these two opposing processes. In fall and winter, the DIC flux due to vertical advection dominates over the Ekman transport (Figure S14 in Supporting Information S1). In winter, however, stronger winds drive an increase in the Ekman flux of DIC, which continues until the net advection of DIC changes sign around the beginning of spring.

In the ASZ, seasonal variability in the advective flux of DIC from the SIZ is essential to explain the carbon air-sea fluxes in the region. In the annually integrated view, the net advective flux in the ASZ is the residual between DIC removal from lateral advection at the northern front and DIC supply by both vertical advection and horizontal advection from the SIZ (Figure 3). The different components of the advective flux depend on both the circulation and the DIC concentration of the source waters. These two aspects are connected but could evolve independently under future warming. For example, ice retreat could increase wintertime outgassing in the SIZ, subsequently reducing the northward Ekman flux of DIC and carbon outgassing in the ASZ. In the seasonal picture, the net advective flux of DIC is smaller in magnitude than some of the other fluxes (Figure 3). Still, the change in sign of the net advection from periods of outgassing to uptake, which is due to a decrease in the amount of DIC entering from the SIZ by Ekman transport (Figure S13 in Supporting Information S1), implies that wind-driven advection of DIC from the seasonal ice zone plays an important role in driving carbon outgassing in the ACC.

It is challenging to compare these results with previous work as there has been no other observation-based circumpolar mixed layer DIC budget in the Southern Ocean. However, a regional study of the Weddell Gyre (part of the SIZ) based on shipboard data and an inverse model found that DIC entrained from below mostly exits the gyre through northward transport to the ACC frontal region (equivalent to the ASZ) or becomes deep water at the gyre edges (Brown et al., 2015). Using the same biogeochemical float data set as this work, Prend, Gray, et al. (2022) find a strong role of the entrainment of carbon-rich waters into the mixed layer to explain spatial variability in carbon outgassing. However, they focus on inter-basin variations in air-sea fluxes, and specifically the period of obduction (the 2 months preceding the maximum mixed layer depth). Comparison to model-based DIC budgets is also difficult since they are typically computed over fixed depths, and many models have seasonal variations in air-sea carbon fluxes that are inconsistent with observations (Mongwe et al., 2018). Still, two recent papers found that the advective flux of DIC plays an important role in the carbon budget of the region (Carroll et al., 2022; Rosso et al., 2017). For example, Carroll et al. (2022) find that the DIC tendency and interannual variability in their SIZ biome is dominated by net advection, although they do not show the contribution from the different advective components. Rosso et al. (2017) do separate the advection into vertical, geostrophic and ageostrophic components, however, they compute their budget down to 650 m, which implicitly reduces the relative importance of Ekman transport (which only occurs in the top ~80 m). One study did find, using a high-resolution model, that Ekman transport was the primary mechanism for the zonally integrated, cross-frontal transport of anthropogenic $\mathrm{CO_2}$ and its intra-annual variability, particularly across the Polar Front (Ito et al., 2010).

While these studies support our own results, they do not directly confirm the importance of Ekman transport from the SIZ in driving carbon outgassing in the southern ACC. In fact, while estimates based on

biogeochemical float data find net outgassing in the high-latitude Southern Ocean that peaks in winter (Gray et al., 2018), this result disagrees with data products based on pCO$_2$ measurements from the Surface Ocean CO$_2$ Atlas (SOCAT) data set (Landschützer et al., 2014; Takahashi et al., 2009), airborne measurements (Long et al., 2021) and ocean biogeochemical circulation models (Hauck et al., 2020). We use the carbon air-sea flux estimates from the SeaFlux ensemble, which is based on 6 fCO$_2$ observation-based data products (Fay et al., 2021; Gregor & Fay, 2021), as input in our analysis in order to further investigate how a carbon uptake signal would combine with the subsurface carbon fluxes provided by the depth-resolved float data, in the optimization process (see Section 3.4). The SeaFlux ensemble includes three neural network-derived products, a mixed layer scheme, a multiple linear regression and a machine learning ensemble, all of which are based on the SOCAT observations.

Inputting the SeaFlux-based air-sea fluxes into our mixed-layer budget leads to mixing and biological fluxes, identified by the optimization scheme, that are not in line with previously published estimates (Figures S10–S12 in Supporting Information S1). In the SIZ, the mixing flux is very small due to a vertical eddy diffusivity that is one order of magnitude smaller than for the ASZ. The error bar also extend significantly into negative values which would indicate diffusive mixing towards regions of higher concentration. In the ASZ, the annually integrated biological flux at 2.65 mol C m^{-2} yr^{-1} is higher than expected based on previous estimates (Figure S10 in Supporting Information S1) (Arteaga et al., 2019). These results seem to imply that carbon uptake of the magnitude found in the SeaFlux-based air-sea fluxes is not consistent with the subsurface DIC fluxes, as well as with the surface and subsurface O$_2$ fluxes provided by the floats. This discrepancy could be due, at least in part, to the availability of year-round float data, whereas SOCAT observations tend to be seasonally biased except in Drake Passage. As carbon air-sea fluxes have been shown to be zonally asymmetric in the Southern Ocean (Gregor et al., 2018; MacGilchrist et al., 2019; Prend, Gray, et al., 2022), differences in the spatial sampling between data sets could also lead to this discrepancy. For example, it is possible that the float data set is capturing different scales of variability that are not resolved in the SOCAT based products. As such, it would be useful to quantify the mixed layer DIC budget in this region on smaller spatial scales (e.g. inter-basin comparisons). However, this is not possible using the approach presented here with the current data coverage, and is a limitation of this study. Determining the mechanisms that drive carbon air-sea flux variability is necessary to understand the discrepancies between different estimates of the Southern Ocean carbon sink from observation-based products and models. Float data, and the subsurface information they provide, are thus an invaluable tool to investigate the drivers of air-sea carbon flux on annual to seasonal timescales.

6. Conclusion

This study uses 6 years of under-ice capable autonomous biogeochemical float data to construct a monthly mixed layer carbon budget in two regions of the high-latitude Southern Ocean. We find that the monthly changes in the mixed layer DIC concentration closely corresponds to the seasonal variations in the biological flux of DIC. However, northward Ekman transport from the SIZ is also significant in setting the seasonal changes in DIC concentration. On annual timescales, mixing with carbon-rich waters from below the mixed layer leads to carbon outgassing in both regions under study (Figure 6). However, in the SIZ, where ice cover damps air-sea exchange and primary production is heavily light-limited, most of the carbon injected from below the mixed layer is transported northward to the ASZ by Ekman advection. In other words, Ekman transport of DIC from the seasonal ice zone contributes to carbon outgassing in the southern portion of the ACC. This has implications for the response of the Southern Ocean carbon cycle to anthropogenic forcing, since reduced ice cover under ocean warming could potentially lead to a redistribution of carbon outgassing from the ASZ to the SIZ.

These results comprise the first observation-based carbon budget spanning large spatial scales and at monthly resolution in the high-latitude Southern Ocean. Strong seasonal variability in air-sea fluxes, as well as biological and advective fluxes of carbon, highlight the importance of year-round measurements in understanding carbon cycling in the region. These results also provide a much-needed observational baseline to evaluate the performance of climate models, which are notably unsuccessful in reproducing the Southern Ocean carbon cycle (Hauck et al., 2020). Improved understanding of these processes is crucial given the key role of the Southern Ocean in the global climate system.
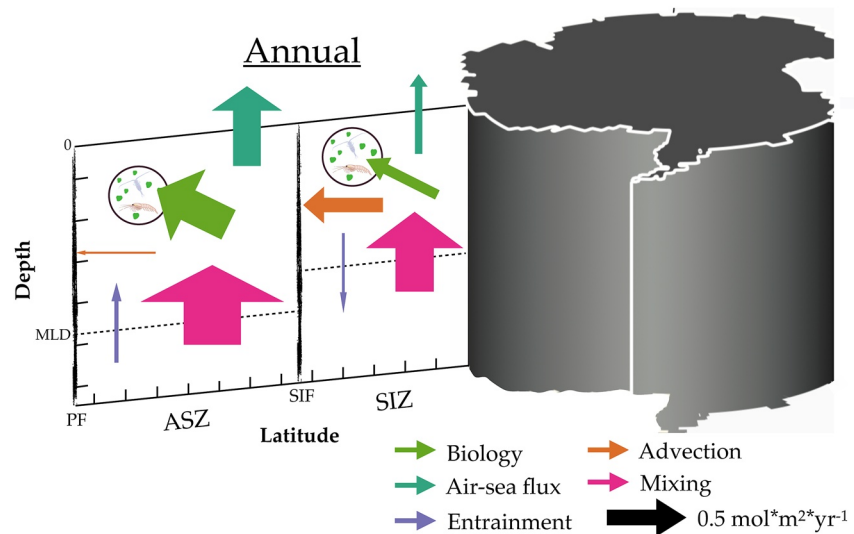
Figure 6. Schematic of the annually integrated fluxes of carbon where each colored arrow corresponds to a different process by which the dissolved inorganic carbon (DIC) content of the mixed layer can be modified. The green arrow represents the net effect of biological activity on mixed layer DIC content or the transfer of carbon between the inorganic and organic carbon (represented by the symbols in the circle) content of the mixed layer. The teal arrow represents the air-sea flux of carbon. The purple arrow corresponds to the entrainment flux of DIC. The orange arrow represents the net advective flux of DIC by Ekman, geostrophic and vertical advection. The pink arrow represents the eddy-driven mixing flux of DIC. The width of each arrow scales with the magnitude of the flux. (ASZ: Antarctic Southern Zone, SIZ: Sea Ice Zone).

Appendix A: Additional Method Information

A1. Horizontal Mass Transport

The monthly averaged Ekman mass transport is northward at the SIE and PF which is as expected due to the presence of strong westerly winds at those latitudes (Figure S4 in Supporting Information S1). The monthly Ekman transport averages to 20.2 Sv at the SIE and 36.5 Sv at the PF, which is consistent with previous modeling studies that found a zonally integrated Ekman transport along 60°S (50°S) of 25 Sv (55 Sv) (Hallberg & Gnanadesikan, 2006). There is about twice as much transport (varying from 1.5× to 2.8×) across the PF than the SIE, which is not surprising as wind driven transport can be inhibited by the presence of sea ice.

Monthly averaged mixed layer geostrophic transport is southward for the SIE and the PF, and it is one order of magnitude smaller than the monthly averaged Ekman transport, with an average of −2.4 Sv ((panel b) of Figure S4 in Supporting Information S1). We present mixed layer geographic transport separately for each zonal region on either side of one boundary due to our choice of depth of integration. In the Ekman transport calculation, we assume that the Ekman depth is shallower than the mixed layer depth, an assumption which is likely true for most months but may break down in summer or fall depending on the eddy viscosity (not shown). This assumption allows us to consider the full depth of the Ekman layer and removes the need to choose a depth of integration. For the geostrophic transport calculation, we integrate the geostrophic velocity down to the mixed layer depth of the region under consideration.

We do not consider the eddy component of the horizontal advection in this region as it has been shown to be more than 50% smaller than the time mean component in the Ekman layer (Dufour et al., 2015).

A2. Mass Budget and Vertical Velocity

The seasonal cycle of the monthly averaged mixed layer mass fluxes differs between the ASZ and the SIZ (Figure S6 in Supporting Information S1). However, we observe that there is a balance between the surface flux of mass and the advective mass flux in both zonal regions while the term representing the difference between the tendency and the entrainment (TEND−$F_{entrain}$) is negligible. In the ASZ, the fluxes of mass do not vary strongly from

month to month. Surface fluxes of mass, including precipitation, evaporation and a small contribution from sea ice melt and freeze, lead to water accumulating in the region's mixed layer. This is balanced by a mass advection out of the ASZ. The sign of the advective flux is set by a balance between the negative Ekman advection and the positive vertical advection. The geostrophic advection is at least one order of magnitude smaller. In the SIZ, the sea ice melt and freeze cycle creates strong seasonal variations in the monthly averaged surface flux which leads to seasonal variations of similar magnitude but opposite sign in the advective flux. As such, we see a positive advective flux of mass (driven by vertical advection) during ice formation and a negative advective mass flux (driven by Ekman advection) during sea ice melt. On annual time scales, mass fluxes in the SIZ and the ASZ are similar with a positive surface flux opposed by a negative advective flux driven by a dominance of Ekman transport out of the zone over vertical mass advection into the mixed layer (Figure S7 in Supporting Information S1).

Using the mixed layer mass budget, we solve for the vertical velocity at the base of the mixed layer (w_{-h}) which is shown in Figure S3 in Supporting Information S1. We find an average w_{-h} of 1.19×10^{-6} m/s (1.07×10^{-6} m/s) in the ASZ (SIZ). This vertical velocity is of the expected scale and sign for these two zonal regions where upwelling is expected (Gruber et al., 2019). Because we have used a mass budget to estimate w_{-h}, our estimate includes both the effect of Ekman upwelling and other processes such as topography-driven or storm-driven upwelling.

A3. Estimated Parameters

We solve a non-linear system composed of the different monthly averaged budget equations for DIC and O_2 to find the missing parameters: the eddy diffusivity (κ_z), the respiration quotient (R_{O_2}) and the monthly biological flux of DIC (F_{bio}). We find an eddy diffusivity of $(6.83 \pm 5.8) \times 10^{-5}$ m^2 s^{-1} ($(2.95 \pm 2.5) \times 10^{-5}$ m^2 s^{-1}) for the ASZ (SIZ) (see Sections 3.5 and 5 for more information). We find a respiratory quotient of -0.65 ± 0.16 (-1.59 ± 0.26) for the ASZ (SIZ). The canonical value for the oxygen to carbon ratio is -1.45 (Anderson & Sarmiento, 1994). However, DeVries and Deutsch (2014) found important latitudinal variations in the amount of oxygen consumed by unit of phosphate released during respiration $\left(R_{O_2/P}\right)$. In the high-latitude Southern Ocean in particular, they find that $R_{O_2/P}$ increases from about 50 to 200 between 47°S and 70°S. When we convert $R_{O_2/P}$ to the respiratory quotient $\left(R_{O_2/C}\right)$ using 106C:P, we find that we see a latitudinal variation of similar magnitude from the ASZ to the SIZ. The magnitude of the monthly averaged biological flux of DIC obtained from the optimization scheme and its clear seasonal cycle are as expected with a strong uptake of carbon during the spring bloom, stronger in the ASZ than in the SIZ (Figure S5 in Supporting Information S1). The positive flux of carbon in winter, indicating dominance of respiration over photosynthesis, can be explained by the severe light and micro-nutrient limitations in the high-latitude Southern Ocean.

A4. Error and Correlation of Each Variable Used in the Monte Carlo Simulation

We record the error and correlation of each variable used in the Monte Carlo simulation in Table A1.

Table A1
Error and Correlation of Each Variable Used in Monte Carlo Simulation

Variable	Error	Unit	Correlation	Source
T	0.002	°C	Uncorrelated	(Wong et al., 2020)
S	0.01	PSU	Uncorrelated	(Wong et al., 2020)
P	2.4	dbar	Uncorrelated	(Wong et al., 2020)
O_2	3	μmol/kg	Uncorrelated	(Johnson et al., 2017)
TA	8.74*	μmol/kg	Uncorrelated	(Carter et al., 2018)
pH	0.007	total	Uncorrelated	(Johnson et al., 2017)
N	0.5	μmol/kg	Uncorrelated	(Johnson et al., 2017)
ΔSIC$_{SIZ}$	3.45×10^8*	m^2/day	Uncorrelated	(Hersbach et al., 2020)
ΔSIC$_{ASZ}$	4.23×10^7*	m^2/day	Uncorrelated	(Hersbach et al., 2020)
SIT	20%	N/A	Uncorrelated	(H. Li et al., 2018)

Table A1
Continued

Variable	Error	Unit	Correlation	Source
SI transport	20%	N/A	Uncorrelated	
SIh	20%	N/A	Uncorrelated	
(Precip. - Evap.)	1.24×10^{-7}*	kg/m^2/s	Uncorrelated	(Hersbach et al., 2020)
$(\tau_x/\rho f)_{inter}$	0.00246*	m^2/s	Uncorrelated	(Hersbach et al., 2020)
$(\tau_y/\rho f)_{inter}$	0.00167*	m^2/s	Uncorrelated	(Hersbach et al., 2020)
$\vec{u}_{geo-inter}$	20%	N/A	Uncorrelated	(Gray & Riser, 2014)
$F_{air-sea-C}$	0.506*	mol/m^2/yr	Correlated in time	(Gray et al., 2018)
$F_{air-sea-O_2}$	20%	N/A	Correlated in time	(Bushinsky et al., 2017)

Note. *average error from field of individual errors.

Data Availability Statement

The Southern Ocean Carbon and Climate Observations and Modeling (SOCCOM) snapshot of quality-controlled data from 22 December 2020 (Southern Ocean Carbon and Climate Observations and Modeling Project, 2021) is available from the SOCCOM project at http://doi.org/10.6075/J0B27ST5. We also utilize the European Centre for Carbon Medium-Range Weather Forecasts (ECMWF) ERA5 atmospheric reanalysis product (Hersbach et al., 2021) and the Ocean Reanalysis System 5 (ORAS5) (Copernicus Climate Change Service, 2021) both available at https://cds.climate.copernicus.eu/. Other data sets used include the SeaFlux harmonized sea-air CO_2 fluxes (Gregor & Fay, 2021) available at https://doi.org/10.5281/zenodo.5482547, the Roemmich-Gilson Argo Climatology (Roemmich & Gilson, 2009), available at https://sio-argo.ucsd.edu/RG_Climatology.html and based on the Argo data (Argo, 2021), and the ETOPO1 Global Relief Model (NOAA National Geophysical Data Center, 2009) available at http://dx.doi.org/10.7289/V5C8276M.

References

Amante, C., & Eakins, B. (2009). *ETOPO1 1 arc-minute global relief model: Procedures, data sources and analysis* (Tech. Rep.). National Geophysical Data Center, NOAA. https://doi.org/10.7289/V5C8276M

Anderson, L. A., & Sarmiento, J. L. (1994). Redfield ratios of remineralization determined by nutrient data analysis. *Global Biogeochemical Cycles*, *8*(1), 65–80. https://doi.org/10.1029/93GB03318

Argo. (2021). Argo float data and metadata from global data assembly center (ARGO GDAC) [Dataset]. Argo. https://doi.org/10.17882/42182

Arteaga, L. A., Pahlow, M., Bushinsky, S. M., & Sarmiento, J. L. (2019). Nutrient controls on export production in the southern ocean. *Global Biogeochemical Cycles*, *33*(8), 942–956. https://doi.org/10.1029/2019GB006236

Balch, W. M., Bates, N. R., Lam, P. J., Twining, B. S., Rosengard, S. Z., Bowler, B. C., et al. (2016). Factors regulating the great calcite belt in the southern ocean and its biogeochemical significance. *Global Biogeochemical Cycles*, *30*(8), 1124–1144. https://doi.org/10.1002/2016GB005414

Branch, M. A., Coleman, T. F., & Li, Y. (1999). A subspace, interior, and conjugate gradient method for large-scale bound-constrained minimization problems. *SIAM Journal on Scientific Computing*, *21*(1), 1–23. https://doi.org/10.1137/S1064827595289108

Briggs, E. M., Martz, T. R., Talley, L. D., Mazloff, M. R., & Johnson, K. S. (2018). Physical and biological drivers of biogeochemical tracers within the seasonal Sea Ice zone of the southern ocean from profiling floats. *Journal of Geophysical Research: Oceans*, *123*(2), 746–758. https://doi.org/10.1002/2017JC012846

Bronselaer, B., Zanna, L., Munday, D. R., & Lowe, J. (2018). Southern ocean carbon-wind stress feedback. *Climate Dynamics*, *51*(7), 2743–2757. https://doi.org/10.1007/s00382-017-4041-y

Brown, P. J., Jullion, L., Landschützer, P., Bakker, D. C. E., Naveira Garabato, A. C., Meredith, M. P., et al. (2015). Carbon dynamics of the Weddell Gyre, southern ocean. *Global Biogeochemical Cycles*, *29*(3), 288–306. https://doi.org/10.1002/2014GB005006

Bushinsky, S. M., & Cerovečki, I. (2023). Subantarctic mode water biogeochemical formation properties and interannual variability. *AGU Advances*, *4*(2), e2022AV000722. https://doi.org/10.1029/2022AV000722

Bushinsky, S. M., Gray, A. R., Johnson, K. S., & Sarmiento, J. L. (2017). Oxygen in the southern ocean from argo floats: Determination of processes driving air-sea fluxes. *Journal of Geophysical Research: Oceans*, *122*(11), 8661–8682. https://doi.org/10.1002/2017JC012923

Bushinsky, S. M., Landschützer, P., Rödenbeck, C., Gray, A. R., Baker, D., Mazloff, M. R., et al. (2019). Reassessing southern ocean air-sea CO_2 flux estimates with the addition of biogeochemical float observations. *Global Biogeochemical Cycles*, *33*(11), 1370–1388. https://doi.org/10.1029/2019GB006176

Butterworth, B. J., & Miller, S. D. (2016). Air-sea exchange of carbon dioxide in the southern ocean and Antarctic marginal ice zone. *Geophysical Research Letters*, *43*(13), 7223–7230. https://doi.org/10.1002/2016GL069581

Carroll, D., Menemenlis, D., Dutkiewicz, S., Lauderdale, J. M., Adkins, J. F., Bowman, K. W., et al. (2022). Attribution of space-time variability in global-ocean dissolved inorganic carbon. *Global Biogeochemical Cycles*, *36*(3), e2021GB007162. https://doi.org/10.1029/2021GB007162

Carter, B. R., Feely, R. A., Williams, N. L., Dickson, A. G., Fong, M. B., & Takeshita, Y. (2018). Updated methods for global locally interpolated estimation of alkalinity, pH, and nitrate. *Limnology and Oceanography: Methods*, *16*(2), 119–131. https://doi.org/10.1002/lom3.10232

Coggins, A., Watson, A. J., Schuster, U., Mackay, N., King, B., McDonagh, E., & Poulton, A. J. (2023). Surface ocean carbon budget in the 2017 South Georgia diatom bloom: Observations and validation of profiling biogeochemical argo floats. *Deep Sea Research Part II: Topical Studies in Oceanography*, *209*, 105275. https://doi.org/10.1016/j.dsr2.2023.105275

Copernicus Climate Change Service, C. D. S. (2021). Oras5 global ocean reanalysis monthly data from 1958 to present [Dataset]. Copernicus Climate Change Service (C3S) Climate Data Store (CDS). https://doi.org/10.24381/cds.67e8eeb7

Cronin, M. F., Pelland, N. A., Emerson, S. R., & Crawford, W. R. (2015). Estimating diffusivity from the mixed layer heat and salt balances in the North Pacific. *Journal of Geophysical Research: Oceans*, *120*(11), 7346–7362. https://doi.org/10.1002/2015JC011010

de Boyer Montégut, C., Madec, G., Fischer, A. S., Lazar, A., & Iudicone, D. (2004). Mixed layer depth over the global ocean: An examination of profile data and a profile-based climatology. *Journal of Geophysical Research*, *109*(C12), C12003. https://doi.org/10.1029/2004JC002378

DeVries, T. (2014). The oceanic anthropogenic CO_2 sink: Storage, air-sea fluxes, and transports over the industrial era. *Global Biogeochemical Cycles*, *28*(7), 631–647. https://doi.org/10.1002/2013GB004739

DeVries, T., & Deutsch, C. (2014). Large-scale variations in the stoichiometry of marine organic matter respiration. *Nature Geoscience*, *7*(12), 890–894. https://doi.org/10.1038/ngeo2300

Dickson, A. G. (1990). Standard potential of the reaction: AgCl(s) + 12H$_2$(g) = Ag(s) + HCl(aq), and and the standard acidity constant of the ion HSO$_4$- in synthetic sea water from 273.15 to 318.15 K. *The Journal of Chemical Thermodynamics*, *22*(2), 113–127. https://doi.org/10.1016/0021-9614(90)90074-Z

Dove, L. A., Balwada, D., Thompson, A. F., & Gray, A. R. (2022). Enhanced ventilation in energetic regions of the Antarctic circumpolar current. *Geophysical Research Letters*, *49*(13), e2021GL097574. https://doi.org/10.1029/2021GL097574

Dufour, C. O., Griffies, S. M., de Souza, G. F., Frenger, I., Morrison, A. K., Palter, J. B., et al. (2015). Role of mesoscale eddies in cross-frontal transport of heat and biogeochemical tracers in the southern ocean. *Journal of Physical Oceanography*, *45*(12), 3057–3081. https://doi.org/10.1175/JPO-D-14-0240.1

Dufour, C. O., Sommer, J. L., Gehlen, M., Orr, J. C., Molines, J.-M., Simeon, J., & Barnier, B. (2013). Eddy compensation and controls of the enhanced sea-to-air CO_2 flux during positive phases of the Southern Annular Mode. *Global Biogeochemical Cycles*, *27*(3), 950–961. https://doi.org/10.1002/gbc.20090

Fay, A. R., Gregor, L., Landschützer, P., McKinley, G. A., Gruber, N., Gehlen, M., et al. (2021). Harmonization of global surface ocean pCO$_2$ mapped products and their flux calculations; an improved estimate of the ocean carbon sink. *Earth System Science Data Discussions*, 1–32.

Fay, A. R., & McKinley, G. A. (2021). Observed regional fluxes to constrain modeled estimates of the ocean carbon sink. *Geophysical Research Letters*, *48*(20), e2021GL095325. https://doi.org/10.1029/2021GL095325

Friedlingstein, P., Jones, M. W., O'Sullivan, M., Andrew, R. M., Bakker, D. C. E., Hauck, J., et al. (2022). Global carbon budget 2021. *Earth System Science Data*, *14*(4), 1917–2005. https://doi.org/10.5194/essd-14-1917-2022

Gloege, L., McKinley, G. A., Landschützer, P., Fay, A. R., Frölicher, T. L., Fyfe, J. C., et al. (2021). Quantifying errors in observationally based estimates of ocean carbon sink variability. *Global Biogeochemical Cycles*, *35*(4), e2020GB006788. https://doi.org/10.1029/2020GB006788

Gray, A. R., Johnson, K. S., Bushinsky, S. M., Riser, S. C., Russell, J. L., Talley, L. D., et al. (2018). Autonomous biogeochemical floats detect significant carbon dioxide outgassing in the high-latitude southern ocean. *Geophysical Research Letters*, *45*(17), 9049–9057. https://doi.org/10.1029/2018GL078013

Gray, A. R., & Riser, S. C. (2014). A global analysis of sverdrup balance using absolute geostrophic velocities from argo. *Journal of Physical Oceanography*, *44*(4), 1213–1229. https://doi.org/10.1175/JPO-D-12-0206.1

Gregor, L., & Fay, A. (2021). SeaFlux: Harmonised sea-air CO_2 fluxes from surface pCO$_2$ data products using a standardised approach [Dataset]. Zenodo. https://doi.org/10.5281/zenodo.5482547

Gregor, L., Kok, S., & Monteiro, P. M. S. (2018). Interannual drivers of the seasonal cycle of CO_2 in the southern ocean. *Biogeosciences*, *15*(8), 2361–2378. https://doi.org/10.5194/bg-15-2361-2018

Gruber, N., Landschützer, P., & Lovenduski, N. S. (2019). The variable southern ocean carbon sink. *Annual Review of Marine Science*, *11*(1), 159–186. https://doi.org/10.1146/annurev-marine-121916-063407

Gupta, M., Follows, M. J., & Lauderdale, J. M. (2020). The effect of Antarctic sea ice on southern ocean carbon outgassing: Capping versus light attenuation. *Global Biogeochemical Cycles*, *34*(8), e2019GB006489. https://doi.org/10.1029/2019GB006489

Hallberg, R., & Gnanadesikan, A. (2006). The role of eddies in determining the structure and response of the wind-driven southern hemisphere overturning: Results from the Modeling Eddies in the Southern Ocean (MESO) project. *Journal of Physical Oceanography*, *36*(12), 2232–2252. https://doi.org/10.1175/jpo2980.1

Hauck, J., Nissen, C., Landschützer, P., Rödenbeck, C., Bushinsky, S., & Olsen, A. (2023). Sparse observations induce large biases in estimates of the global ocean CO_2 sink: An ocean model subsampling experiment. *Philosophical Transactions of the Royal Society A: Mathematical, Physical & Engineering Sciences*, *381*(2249), 20220063. https://doi.org/10.1098/rsta.2022.0063

Hauck, J., Völker, C., Wang, T., Hoppema, M., Losch, M., & Wolf-Gladrow, D. A. (2013). Seasonally different carbon flux changes in the Southern Ocean in response to the southern annular mode. *Global Biogeochemical Cycles*, *27*(4), 1236–1245. https://doi.org/10.1002/2013GB004600

Hauck, J., Zeising, M., Le Quéré, C., Gruber, N., Bakker, D. C. E., Bopp, L., et al. (2020). Consistency and challenges in the ocean carbon sink estimate for the global carbon budget. *Frontiers in Marine Science*, *7*. https://doi.org/10.3389/fmars.2020.571720

Hersbach, H., Bell, B., Berrisford, P., Biavati, G., Horányi, A., Muñoz Sabater, J., et al. (2021). ERA5 monthly averaged data on single levels from 1940 to present [Dataset]. Copernicus Climate Change Service (C3S) Climate Data Store (CDS). https://doi.org/10.24381/cds.f17050d7

Hersbach, H., Bell, B., Berrisford, P., Hirahara, S., Horányi, A., Muñoz-Sabater, J., et al. (2020). The ERA5 global reanalysis. *Quarterly Journal of the Royal Meteorological Society*, *146*(730), 1999–2049. https://doi.org/10.1002/qj.3803

Holte, J., & Talley, L. (2009). A new algorithm for finding mixed layer depths with applications to argo data and subantarctic mode water formation. *Journal of Atmospheric and Oceanic Technology*, *26*(9), 1920–1939. https://doi.org/10.1175/2009JTECHO543.1

Huang, Y., Fassbender, A. J., & Bushinsky, S. M. (2023). Biogenic carbon pool production maintains the southern ocean carbon sink. *Proceedings of the National Academy of Sciences*, *120*(18), e2217909120. https://doi.org/10.1073/pnas.2217909120

Humphreys, M. P., Schiller, A. J., Sandborn, D. E., Gregor, L., Pierrot, D., van Heuven, S. M. A. C., et al. (2021). PyCO2SYS: Marine carbonate system calculations in Python [Software]. *Zenodo*. https://doi.org/10.5281/zenodo.3744275

Ito, T., Woloszyn, M., & Mazloff, M. (2010). Anthropogenic carbon dioxide transport in the Southern Ocean driven by Ekman flow. *Nature*, *463*(7277), 80–83. https://doi.org/10.1038/nature08687

Jersild, A., & Ito, T. (2020). Physical and biological controls of the drake passage pCO$_2$ variability. *Global Biogeochemical Cycles*, *34*(9), e2020GB006644. https://doi.org/10.1029/2020GB006644

Johnson, K. S., Plant, J. N., Coletti, L. J., Jannasch, H. W., Sakamoto, C. M., Riser, S. C., et al. (2017). Biogeochemical sensor performance in the SOCCOM profiling float array. *Journal of Geophysical Research: Oceans*, *122*(8), 6416–6436. https://doi.org/10.1002/2017JC012838

Jouandet, M. P., Blain, S., Metzl, N., Brunet, C., Trull, T. W., & Obernosterer, I. (2008). A seasonal carbon budget for a naturally iron-fertilized bloom over the Kerguelen Plateau in the Southern Ocean. *Deep Sea Research Part II: Topical Studies in Oceanography*, *55*(5), 856–867. https://doi.org/10.1016/j.dsr2.2007.12.037

Kern, S., & Spreen, G. (2015). Uncertainties in Antarctic sea-ice thickness retrieval from ICESat. *Annals of Glaciology*, *56*(69), 107–119. https://doi.org/10.3189/2015AoG69A736

Krumhardt, K. M., Long, M. C., Lindsay, K., & Levy, M. N. (2020). Southern ocean calcification controls the global distribution of alkalinity. *Global Biogeochemical Cycles*, *34*(12), e2020GB006727. https://doi.org/10.1029/2020GB006727

Landschützer, P., Gruber, N., Bakker, D. C. E., & Schuster, U. (2014). Recent variability of the global ocean carbon sink. *Global Biogeochemical Cycles*, *28*(9), 927–949. https://doi.org/10.1002/2014GB004853

Law, C. S., Abraham, E. R., Watson, A. J., & Liddicoat, M. I. (2003). Vertical eddy diffusion and nutrient supply to the surface mixed layer of the Antarctic Circumpolar Current. *Journal of Geophysical Research C: Oceans*, *108*(8), 28–31. https://doi.org/10.1029/2002JC001604

Lee, K., Kim, T.-W., Byrne, R. H., Millero, F. J., Feely, R. A., & Liu, Y.-M. (2010). The universal ratio of boron to chlorinity for the North Pacific and North Atlantic Oceans. *Geochimica et Cosmochimica Acta*, *74*(6), 1801–1811. https://doi.org/10.1016/j.gca.2009.12.027

Levy, M., Bopp, L., Karleskind, P., Resplandy, L., Ethe, C., & Pinsard, F. (2013). Physical pathways for carbon transfers between the surface mixed layer and the ocean interior. *Global Biogeochemical Cycles*, *27*(4), 1001–1012. https://doi.org/10.1002/gbc.20092

Li, H., Xie, H., Kern, S., Wan, W., Ozsoy, B., Ackley, S., & Hong, Y. (2018). Spatio-temporal variability of Antarctic sea-ice thickness and volume obtained from ICESat data using an innovative algorithm. *Remote Sensing of Environment*, *219*, 44–61. https://doi.org/10.1016/j.rse.2018.09.031

Li, Y., Church, J. A., McDougall, T. J., & Barker, P. M. (2022). Sensitivity of observationally based estimates of ocean heat content and thermal expansion to vertical interpolation schemes. *Geophysical Research Letters*, *49*(24), e2022GL101079. https://doi.org/10.1029/2022GL101079

Long, M. C., Stephens, B. B., McKain, K., Sweeney, C., Keeling, R. F., Kort, E. A., et al. (2021). Strong southern ocean carbon uptake evident in airborne observations. *Science*, *374*(6572), 1275–1280. https://doi.org/10.1126/science.abi4355

Lueker, T. J., Dickson, A. G., & Keeling, C. D. (2000). Ocean pCO_2 calculated from dissolved inorganic carbon, alkalinity, and equations for K1 and K2: Validation based on laboratory measurements of CO_2 in gas and seawater at equilibrium. *Marine Chemistry*, *70*(1), 105–119. https://doi.org/10.1016/S0304-4203(00)00022-0

MacGilchrist, G. A., Naveira Garabato, A. C., Brown, P. J., Jullion, L., Bacon, S., Bakker, D. C., et al. (2019). Reframing the carbon cycle of the subpolar southern ocean. *Science Advances*, *5*(8), 1–8. https://doi.org/10.1126/sciadv.aav6410

Mackay, N., & Watson, A. (2021). Winter Air-Sea CO_2 fluxes constructed from summer observations of the polar southern ocean suggest weak outgassing. *Journal of Geophysical Research: Oceans*, *126*(5), e2020JC016600. https://doi.org/10.1029/2020JC016600

Maurer, T. L., Plant, J. N., & Johnson, K. S. (2021). Delayed-mode quality control of oxygen, nitrate, and pH data on SOCCOM biogeochemical profiling floats. *Frontiers in Marine Science*, *8*, 1118. https://doi.org/10.3389/fmars.2021.683207

McDougall, T., & Barker, P. (2011). *Getting started with TEOS-10 and the Gibbs Seawater (GSW) oceanographic toolbox* (28pp.). SCOR/IAPSO WG127. ISBN 978-0-646-55621-5. Retrieved from https://www.teos-10.org/pubs/Getting_Started.pdf

McNeil, B. I., & Tilbrook, B. (2009). A seasonal carbon budget for the sub-Antarctic Ocean, South of Australia. *Marine Chemistry*, *115*(3), 196–210. https://doi.org/10.1016/j.marchem.2009.08.006

Merlivat, L., Boutin, J., & Antoine, D. (2015). Roles of biological and physical processes in driving seasonal air-sea CO_2 flux in the Southern Ocean: New insights from CARIOCA pCO_2. *Journal of Marine Systems*, *147*(SI), 9–20. https://doi.org/10.1016/j.jmarsys.2014.04.015

Mongwe, N. P., Vichi, M., & Monteiro, P. M. S. (2018). The seasonal cycle of pCO_2 and CO_2 fluxes in the Southern Ocean: Diagnosing anomalies in CMIP5 Earth system models. *Biogeosciences*, *15*(9), 2851–2872. https://doi.org/10.5194/bg-15-2851-2018

Munro, D. R., Lovenduski, N. S., Stephens, B. B., Newberger, T., Arrigo, K. R., Takahashi, T., et al. (2015). Estimates of net community production in the Southern Ocean determined from time series observations (2002–2011) of nutrients, dissolved inorganic carbon, and surface ocean pCO_2 in Drake Passage. *Deep Sea Research Part II: Topical Studies in Oceanography*, *114*, 49–63. https://doi.org/10.1016/j.dsr2.2014.12.014

NOAA National Geophysical Data Center. (2009). Etopo1 1 arc-minute global relief model [Dataset]. NOAA National Centers for Environmental Information. https://doi.org/10.24381/cds.f17050d7

Orsi, A. H., Whitworth, T., & Nowlin, W. D. (1995). On the meridional extent and fronts of the Antarctic Circumpolar Current. *Deep Sea Research Part I: Oceanographic Research Papers*, *42*(5), 641–673. https://doi.org/10.1016/0967-0637(95)00021-W

Perez, F. F., & Fraga, F. (1987). Association constant of fluoride and hydrogen ions in seawater. *Marine Chemistry*, *21*(2), 161–168. https://doi.org/10.1016/0304-4203(87)90036-3

Prend, C. J., Gray, A. R., Talley, L. D., Gille, S. T., Haumann, F. A., Johnson, K. S., et al. (2022). Indo-Pacific sector dominates southern ocean carbon outgassing. *Global Biogeochemical Cycles*, *36*(7), e2021GB007226. https://doi.org/10.1029/2021GB007226

Prend, C. J., Hunt, J. M., Mazloff, M. R., Gille, S. T., & Talley, L. D. (2022). Controls on the boundary between thermally and non-thermally driven pCO_2 regimes in the South Pacific. *Geophysical Research Letters*, *49*(9), e2021GL095797. https://doi.org/10.1029/2021GL095797

Roemmich, D., & Gilson, J. (2009). The 2004–2008 mean and annual cycle of temperature, salinity, and steric height in the global ocean from the Argo Program. *Progress in Oceanography*, *82*(2), 81–100. https://doi.org/10.1016/j.pocean.2009.03.004

Rosso, I., Mazloff, M. R., Verdy, A., & Talley, L. D. (2017). Space and time variability of the southern ocean carbon budget. *Journal of Geophysical Research: Oceans*, *122*(9), 7407–7432. https://doi.org/10.1002/2016JC012646

Shadwick, E. H., De Meo, O. A., Schroeter, S., Arroyo, M. C., Martinson, D. G., & Ducklow, H. (2021). Sea ice suppression of CO_2 outgassing in the West Antarctic Peninsula: Implications for the evolving southern ocean carbon sink. *Geophysical Research Letters*, *48*(11), e2020GL091835. https://doi.org/10.1029/2020GL091835

Shadwick, E. H., Trull, T. W., Tilbrook, B., Sutton, A. J., Schulz, E., Trull, T. W., & Sabine, C. L. (2015). Seasonality of biological and physical controls on surface ocean CO_2 from hourly observations at the southern ocean time series site south of Australia. *Global Biogeochemical Cycles*, *29*(2), 223–238. https://doi.org/10.1002/2014gb004906

Southern Ocean Carbon and Climate Observations and Modeling Project. (2021). Entire SOCCOM/UW MBARI float data set [Dataset]. Southern Ocean Carbon and Climate Observations and Modeling Project. https://doi.org/10.6075/J0B27ST5

Takahashi, T., Feely, R. A., Weiss, R. F., Wanninkhof, R. H., Chipman, D. W., Sutherland, S. C., & Takahashi, T. T. (1997). Global air-sea flux of CO_2: An estimate based on measurements of sea–air pCO_2 difference. *Proceedings of the National Academy of Sciences*, *94*(16), 8292–8299. https://doi.org/10.1073/pnas.94.16.8292

Takahashi, T., Olafsson, J., Goddard, J. G., Chipman, D. W., & Sutherland, S. C. (1993). Seasonal variation of CO_2 and nutrients in the high-latitude surface oceans: A comparative study. *Global Biogeochemical Cycles*, *7*(4), 843–878. https://doi.org/10.1029/93GB02263

Takahashi, T., Sutherland, S. C., Sweeney, C., Poisson, A., Metzl, N., Tilbrook, B., et al. (2002). Global sea–air CO_2 flux based on climatological surface ocean pCO_2, and seasonal biological and temperature effects. *Deep Sea Research Part II: Topical Studies in Oceanography*, *49*(9), 1601–1622. https://doi.org/10.1016/S0967-0645(02)00003-6

Takahashi, T., Sutherland, S. C., Wanninkhof, R., Sweeney, C., Feely, R. A., Chipman, D. W., et al. (2009). Climatological mean and decadal change in surface ocean pCO_2, and net sea–air CO_2 flux over the global oceans. *Deep Sea Research Part II: Topical Studies in Oceanography*, *56*(8), 554–577. https://doi.org/10.1016/j.dsr2.2008.12.009

Vihma, T., & Haapala, J. (2009). Geophysics of sea ice in the Baltic Sea: A review. *Progress in Oceanography*, *80*(3), 129–148. https://doi.org/10.1016/j.pocean.2009.02.002

Wanninkhof, R. (2014). Relationship between wind speed and gas exchange over the ocean revisited. *Limnology and Oceanography: Methods*, *12*(6), 351–362. https://doi.org/10.4319/lom.2014.12.351

Wanninkhof, R., Johnson, K., Williams, N., Sarmiento, J., Riser, S., Briggs, E., et al. (2016). An evaluation of pH and NO_3 sensor data from SOCCOM floats and their utilization to develop ocean inorganic carbon products (Tech. Rep.). Retrieved from https://soccom.princeton.edu

Williams, N. L., Juranek, L. W., Feely, R. A., Russell, J. L., Johnson, K. S., & Hales, B. (2018). Assessment of the carbonate chemistry seasonal cycles in the southern ocean from persistent observational platforms. *Journal of Geophysical Research: Oceans*, *123*(7), 4833–4852. https://doi.org/10.1029/2017JC012917

Wong, A. P. S., Wijffels, S. E., Riser, S. C., Pouliquen, S., Hosoda, S., Roemmich, D., et al. (2020). Argo data 1999–2019: Two million temperature-salinity profiles and subsurface velocity observations from a global array of profiling floats. *Frontiers in Marine Science*, *7*, 700. https://doi.org/10.3389/fmars.2020.00700

Wu, Y., Bakker, D. C. E., Achterberg, E. P., Silva, A. N., Pickup, D. D., Li, X., et al. (2022). Integrated analysis of carbon dioxide and oxygen concentrations as a quality control of ocean float data. *Communications Earth & Environment*, *3*(1), 92. https://doi.org/10.1038/s43247-022-00421-w

Wu, Y., & Qi, D. (2022). Inconsistency between ship- and Argo float-based pCO_2 at the intense upwelling region of the Drake Passage, Southern Ocean. *Frontiers in Marine Science*, *9*. https://doi.org/10.3389/fmars.2022.1002398

Yang, B., Shadwick, E. H., Schultz, C., & Doney, S. C. (2021). Annual mixed layer carbon budget for the West Antarctic Peninsula continental shelf: Insights from year-round mooring measurements. *Journal of Geophysical Research: Oceans*, *126*(4), e2020JC016920. https://doi.org/10.1029/2020JC016920

Zeebe, R. E., & Wolf-Gladrow, D. (2001). *CO_2 in seawater: Equilibrium, kinetics, isotopes*. Elsevier.

Zuo, H., Balmaseda, M. A., Tietsche, S., Mogensen, K., & Mayer, M. (2019). The ECMWF operational ensemble reanalysis-analysis system for Ocean and sea ice: A description of the system and assessment. *Ocean Science*, *15*(3), 779–808. https://doi.org/10.5194/os-15-779-2019